Neurobiology of Disease 126 (2019) 124–136

Contents lists available at ScienceDirect

Neurobiology of Disease

journal homepage: www.elsevier.com/locate/ynbdi

Review

Hypoxia promotes tau hyperphosphorylation with associated neuropathology in vascular dysfunction

Limor Raz[a,*], Kiran Bhaskar[a,b], John Weaver[c], Sandro Marini[g], Quanguang Zhang[f], Jeffery F. Thompson[a], Candice Espinoza[a], Sulaiman Iqbal[a], Nicole M. Maphis[b], Lea Weston[b], Laurel O. Sillerud[a,d], Arvind Caprihan[d], John C. Pesko[e], Erik B. Erhardt[e], Gary A. Rosenberg[a]

[a] Department of Neurology, 1 University of New Mexico Health Sciences Center, Albuquerque, NM 87131, United States
[b] Department of Molecular Genetics and Microbiology, 1 University of New Mexico Health Sciences Center, Albuquerque, NM 87131, United States
[c] BRaIN Imaging Center, 1 University of New Mexico Health Sciences Center, Albuquerque, NM 87131, United States
[d] MIND Research Network, 1 University of New Mexico Health Sciences Center, Albuquerque, NM 87131, United States
[e] Department of Mathematics and Statistics, 1 University of New Mexico Health Sciences Center, Albuquerque, NM 87131, United States
[f] Department of Neuroscience and Regenerative Medicine, Department of Neurology, Augusta University, 1120 15th Street, Augusta, GA 30912, United States
[g] Center for Genomic Medicine, Massachusetts General Hospital, 185 Cambridge Street, Boston, MA 02114, United States

ARTICLE INFO

Keywords:
Hypertension
Hypoxia
SHRSP
Tau
Neurodegeneration

ABSTRACT

Background: Hypertension-induced microvascular brain injury is a major vascular contributor to cognitive impairment and dementia. We hypothesized that chronic hypoxia promotes the hyperphosphorylation of tau and cell death in an accelerated spontaneously hypertensive stroke prone rat model of vascular cognitive impairment.

Methods: Hypertensive male rats ($n = 13$) were fed a high salt, low protein Japanese permissive diet and were compared to Wistar Kyoto control rats ($n = 5$).

Results: Using electron paramagnetic resonance oximetry to measure *in vivo* tissue oxygen levels and magnetic resonance imaging to assess structural brain damage, we found compromised gray (dorsolateral cortex: $p = .018$) and white matter (corpus callosum: $p = .016$; external capsule: $p = .049$) structural integrity, reduced cerebral blood flow (dorsolateral cortex: $p = .005$; hippocampus: $p < .001$; corpus callosum: $p = .001$; external capsule: $p < .001$) and a significant drop in cortical oxygen levels ($p < .05$). Consistently, we found reduced oxygen carrying neuronal neuroglobin ($p = .008$), suggestive of chronic cerebral hypoperfusion in high salt-fed rats. We also observed a corresponding increase in free radicals (NADPH oxidase: $p = .013$), p-Tau (pThr231) in dorsolateral cortex ($p = .011$) and hippocampus ($p = .003$), active interleukin-1β ($p < .001$) and neurodegeneration (dorsolateral cortex: $p = .043$, hippocampus: $p = .044$). Human patients with subcortical ischemic vascular disease, a type of vascular dementia ($n = 38$; mean age = 68; male/female ratio = 23/15) showed reduced hippocampal volumes and cortical shrinking ($p < .05$) consistent with the neuronal cell death observed in our hypertensive rat model as compared to healthy controls ($n = 47$; mean age = 63; male/female ratio = 18/29).

Conclusions: Our data support an association between hypertension-induced vascular dysfunction and the

Abbreviations: Aβ, Amyloid Beta; AD, Alzheimer's disease; ADC, apparent diffusion coefficient; ASL, arterial spin labeling; α-SYNUC, α-Synuclein; BBB, blood brain barrier; BP, blood pressure; CAA, Cerebral Amyloid Angiopathy; CBF, cerebral blood flow; CC, Corpus Callosum; CX3CR1, CX3C chemokine receptor 1; DLCTX, Dorsolateral Cortex; DTI, Diffusion tensor imaging; EC, External Capsule; EPR, Electron Paramagnetic Resonance; FA, fractional anisotropy; GM, gray matter; Hgbα, Hemoglobin-α; Hgbβ, Hemoglobin-β; HIF-1α, hypoxia-inducible factor 1-alpha; HIPP, Hippocampus; 4-HNE, 4-hydroxynonenal; HV, hippocampal volume; IL-1β, interleukin-1 beta; JPD, Japanese Permissive Diet; LiPc, lithium phthalocyanine; mCT, mean cortical thickness; MRI, Magnetic Resonance Imaging; NFTs, neurofibrillary tangles; Ngb, neuroglobin; 3-NT, 3-nitrotyrosine; O_2, Oxygen; pO_2, partial pressure of oxygen; p-Tau, Phosphorylated Tau; RNS, reactive nitrogen species; ROS, reactive oxygen species; SHRSP, Spontaneously Hypertensive Stroke Prone Rat; SIVD-BD, Subcortical Ischemic Vascular Disease of the Binswanger type; SVD, small vessel disease; TUNEL, Terminal deoxynucleotidyl transferase dUTP nick end labeling; VCID, Vascular contributor to Cognitive Impairment and Dementia; VOL, Brain volume; W, weeks; WKY, Wistar Kyoto; WM, white matter

* Corresponding author at: 1 University of New Mexico, Albuquerque, NM 87131, United States.
E-mail addresses: dr.liraz@gmail.com (L. Raz), KBhaskar@salud.unm.edu (K. Bhaskar), JMWeaver@salud.unm.edu (J. Weaver), smarini1@mgh.harvard.edu (S. Marini), qzhang@augusta.edu (Q. Zhang), JefThompson@salud.unm.edu (J.F. Thompson), CEspinoza@salud.unm.edu (C. Espinoza), SIqbal@salud.unm.edu (S. Iqbal), NMaphis@salud.unm.edu (N.M. Maphis), llweston@salud.unm.edu (L. Weston), LSillerud@salud.unm.edu (L.O. Sillerud), acaprihan@mrn.org (A. Caprihan), erike@stat.unm.edu (E.B. Erhardt), GRosenberg@salud.unm.edu (G.A. Rosenberg).

https://doi.org/10.1016/j.nbd.2018.07.009
Received 28 February 2018; Received in revised form 11 June 2018; Accepted 10 July 2018
Available online 25 July 2018

sporadic occurrence of phosphorylated tau and cell death in the rat model, correlating with patient brain atrophy, which is relevant to vascular disease.

1. Introduction

Dementia results from the interplay between vascular risk factors, neurodegeneration due to abnormal accumulation of proteins and aging. Neuropathological analysis of human autopsy brains with dementia reveal the combination of amyloid beta (Aβ) plaques and phospho-Tau (p-Tau) accumulation as neurofibrillary tangles (NFTs), which often co-occur with large and/or small infarcts (Robinson et al., 2011). When the vascular underpinning is present, Alzheimer's disease (AD) is often accelerated (Paul et al., 2007). Despite the frequent occurrence of both diseases, the relationship between vascular dysfunction and AD-related tau pathology is poorly understood.

Hypertension is considered to be the major vascular contributor to cognitive impairment and dementia (VCID) and can accelerate AD progression. Recent studies have begun to address the complex molecular interactions linking hypertension-induced cerebrovascular dysfunction with the formation of AD-related proteinopathies. Hypertension damages the arterioles, leading to reduced cerebral blood flow (CBF) and hypoxia (Iadecola & Davisson, 2008). Hyperphosphorylation of tau is reported to cause cell death potentially via microtubule de-stabilization during the later stages of AD (Gendron & Petrucelli, 2009). Lack of O_2 is one of the factors that could drive p-Tau likely via activation of various kinases (Gao et al., 2013). We previously showed that the spontaneously hypertensive and stroke-prone rat (SHRSP) was hypoxic and consequently had a disrupted blood brain barrier (BBB) associated with white matter (WM) damage (Jalal et al., 2012). In the present study, we examined the impact of hypoxia in the SHRSP model on gray matter (GM) neurodegeneration, which could be impacted by p-Tau and lead to cell death, eventually contributing to brain atrophy.

Neuropathological analysis of postmortem human brains with dementia shows early increase and an age-dependent progression in extracellular Aβ deposition followed by intraneuronal accumulation of p-Tau (Villarreal et al., 2014). Increasing numbers of studies also show the deposition of pathologically misfolded proteins in damaged neurovasculature (Kovari et al., 2013; Schreiber et al., 2014). These neuropathological correlates of small vessel disease (SVD) may lead to a chain of events characterized by an exacerbated neuroinflammatory response, alterations in vascular permeability and brain lesions (Schreiber et al., 2012) reflecting neuronal cell loss (Fotuhi et al., 2009; Humpel, 2011; Sironi et al., 2001), which may contribute to VCID (Gorelick et al., 2011; Snyder et al., 2015).

The SHRSP model shows neuropathological features of SVD (Sabbatini et al., 2001). In the prior studies, our group used the SHRSP fed with a Japanese Permissive Diet (JPD) consisting of high salt and low protein along with a permanent unilateral carotid artery occlusion to assess the effect of hypertension and ischemia on various physiological measures. These SHRSP/JPD animals showed extensive WM damage due to hypoxia, BBB opening in WM regions and behavioral changes (Henning et al., 2010; Jalal et al., 2012, 2015). However, it is important to note that since ischemia is not a typical co-morbidity associated with VCID, it is therefore important to assess the effects of JPD alone in SHRSP without a unilateral carotid artery occlusion.

Chronic hypertension in SHRSP alters the cerebrovascular morphology of the micro- and macro- vasculature by disrupting arterial endothelial cell lining, promoting the fibrosis of blood vessel walls and narrowing of lumens (Pires et al., 2013), thus reducing CBF (Yang & Rosenberg, 2011). Under hypoxic conditions, factors responsible for oxidative metabolism may be altered. In particular, neuroglobin (Ngb) is known to bind O_2 and localize to the neuronal mitochondria (Burmester & Hankeln, 2009), serving as a scavenger of reactive oxygen species (ROS) and exerting anti-apoptotic effects (Brittain et al., 2010). Understanding the molecular sequence of events in this novel and highly disease-relevant neuropathological cascade may provide much needed insight into the progression of SVD.

The etiology, pathophysiology and molecular causes of SVD are currently unknown and there is a lack of clinically relevant animal model necessary for mechanistic studies (Gorelick et al., 2011). We hypothesize that chronic hypertension coupled with hypoxia will promote a neuroinflammatory response and induce p-Tau neuropathology, leading to neurodegeneration via the reduction of Ngb. Our findings suggest that chronic hypoperfusion may drive endogenous rat p-Tau in SHRSP/JPD via a downregulation in Ngb, the release of free radicals and the activation of a neuroinflammatory cascade, resulting in BBB permeability and neuronal cell death. The present correlational and longitudinal study establishes a model that closely mimics VCID neuropathology.

2. Materials and methods

2.1. Experimental design

Male SHRSP (n = 13) were purchased (Charles River Laboratories International Inc., Wilmington, MA, USA) at 6 weeks (W) of age, a timepoint associated with emerging hypertensive pathophysiology in the model. Age and strain matched Wistar Kyoto (WKY, n = 5) served as normotensive controls. Animals were randomized into experimental and control groups using a random number generator software. Weekly blood pressure (BP) and weight measurements were recorded throughout the study. A JPD consisting of 16% protein, 0.75% potassium, 4% sodium (Ziegler Bros Inc., Gardeners, PA, USA) with 1% saline in drinking water was initiated at the end of 11 W of age and continued for 4 W until the end of the 15 W of life, at which point all animals were sacrificed. The 15 W timepoint was chosen based on our prior studies showing the appearance of abnormal neurological symptoms and WM lesions on magnetic resonance imaging (MRI) (Jalal et al., 2012). However, the current research will focus on the dorsolateral cortex (DLCTX) and hippocampus (HIPP). A detailed description of the behavioral phenotype and neurological appearance of each rat was recorded during the study. The WKY control group received a standard rodent diet composed of 19% protein, 0.4% potassium, 0.1% sodium and tap water. Female rats were omitted from our studies to avoid confounding hormonal effects.

2.2. Tissue preparation

Rats were sacrificed at the end of 15 W of life. Pentobarbital was used as an anesthetic (50 mg/kg body weight, intraperitoneally) during perfusion, as described (Jalal et al., 2015).

2.2.1. Histological studies

For histological studies, 0.1% procaine in cold phosphate buffer followed by 2% PLP (2% paraformaldehyde, 0.1 mol/L sodium periodate, 75 mmol/L lysine in 100 mmol/L sodium phosphate buffer, pH 7.4) solutions were administered transcardially throughout the perfusion procedure. Brains were then quickly removed and incubated in a 2% PLP solution for 24 h at 4 °C. Tissue preparation for cryosectioning consisted of incubation with a cryoprotecting solution (30% sucrose/2% PLP, 4 °C), tissue insertion into a Peel-A-Way histology mold (Ted Pella Inc., Redding, CA, USA) with Tissue-Tek embedding

medium (OCT; Sakura Finetek, Torrance, CA, USA). Next, the tissue was frozen in 2-methylbutane solution with liquid nitrogen as a cooling solution. Brains were stored at a −80 °C freezer until use and sectioned via a cryostat in 10 μm slices prior to histological analysis. The following antibodies were used in immunochemistry studies: DAB staining - Hemoglobin-α (Hgbα) and Hemoglobin-β (Hgbβ) 1:100 (Santa Cruz Biotechnology Inc., Dallas, TX, USA), AT180 (mouse monoclonal antibody to Tau phosphorylated at T231 residue) 1:750 (Thermo Fisher Scientific Inc., Waltham, MA, USA), α-Synuclein (α-SYNUC) 1:500 (Cell Signaling Technology Inc., Danvers, MA, USA), $A\beta_{1-42}$ (corresponding to amino acids 33–42 of human $A\beta_{1-42}$, able to cross react with rat) 1:200 (Abcam Biotechnology, Cambridge, MA, USA), NeuN 1:400 (Cell Signaling Technology Inc.) were incubated overnight at 4 °C. Secondary biotinylated antibodies: Biotin-SP-conjugated Affinity Pure Goat Anti-Rabbit and Goat Anti-Mouse 1:250 (Jackson ImmunoResearch Laboratories, Inc., West Grove, PA, USA) were incubated for 1 h at RT, as previously described (Maphis et al., 2016). Fluorescence staining - Cy-3-conjugated Affinity Pure Goat Anti-Mouse IgG antibody 1:250 (Jackson ImmunoResearch Laboratories, Inc.), RECA1 1:100 (Abcam Biotechnology), Ngb 1:400 (Cloud-Clone Corp., Katy, TX, USA), CX3C chemokine receptor 1 (CX3CR1, R & D systems, Goat monoclonal, 1:200, blocking was with 5% normal donkey serum), NeuN and $A\beta_{1-42}$ (same antibodies as specified above) were incubated overnight at 4 °C. Secondary antibodies 1:500 (Invitrogen, Waltham, MA, USA), conjugated to FITC (Alexafluor 488), Cy-3 (Alexafluor 546) or mCherry (Alexafluor 597), were incubated at RT for 90 min. 4′-6-Diamidino-2-phenyllinidole (DAPI) staining (Invitrogen) was applied for 10 s per slide for all experiments. 4-hydroxynonenal (4-HNE) immunofluorescence double staining 1:50 (Abcam Biotechnology) was performed for the detection of lipid peroxidation in tissues with a DAPI counterstain. Fluorescence images of 4-HNE were captured on a Zeiss Axiovert 35 fluorescent microscope and analyzed using LSM510 Meta imaging software, as previously described (Lu et al., 2017; Zhang et al., 2009).

2.2.2. Biochemical studies

For Western Blot (WB) studies, rats were perfused with cold saline, the brains were quickly removed and snap-frozen in 2-methylbutane and stored in −80 °C, as previously reported (Jalal et al., 2012). Briefly, frozen brains were sectioned in 400 μm increments and micro-punches were collected at −25 °C from left and right hemispheres in gray matter (GM) (DLCTX, HIPP) and WM (Corpus Callosum (CC), External Capsule (EC)) brain regions. The tissue punches were lysed in EDTA-free RIPA lysis buffer containing Halt protease (Aprotinin, Bestatin, E64, Leupeptin) and phosphatase (Sodium Fluoride, Sodium Orthovanadate, β-glycerophosphate, Sodium Pyrophosphate) inhibitor cocktail (ThermoFisher Scientific, Inc.). Immunoblotting techniques followed standard laboratory procedures. Polyvinylidene fluoride (PVDF) membranes were probed with the following primary antibodies: hypoxia-inducible factor 1-alpha (HIF-1α) 1:1000 (Abcam Biotechnology), interleukin-1 beta (IL-1β) 1:750 (R&D Systems Inc., Minneapolis, MN, USA), Actin 1:7500 (Sigma-Aldrich Inc., St. Louis, MO, USA), Glyceraldehyde-3-phosphate dehydrogenase (GAPDH) 1:10,000 (Sigma-Aldrich Inc., St. Louis, MO, USA), AT180 1:700 (Thermo Fisher Scientific Inc.), Tau5 1:10,000, (Mouse monoclonal, Millipore), 3-nitrotyrosine (3-NT) 1:200 (Santa Cruz Biotechnology Inc.), α-SYNUC 1:2000 (Cell Signaling Technology Inc.). Secondary antibodies for WB: Peroxidase-conjugated Affinity Pure Goat anti-rabbit, anti-mouse or anti-goat 1:20,000 (Jackson ImmunoResearch Laboratories, Inc.). WB band intensities were normalized against actin, which served as loading control. Results were quantified using Image J software.

2.3. Stereology count

Positively stained cells on DAB slides were quantified using an unbiased stereology protocol. StereoInvestigator software (Version 6, MBF Bioscience, Williston, VT, USA) on an Olympus BX-51 microscope controlled a motorized stage. By using the optical fractionator function of the StereoInvestigator program, we counted and averaged the number of p-Tau (AT180), NeuN and Hgb (α and β chains) of positively stained cells in experimental and control groups ($n = 5$ slides/group) in the DLCTX and HIPP (CA1, CA2 and CA3/DG) regions. These brain regions of interest were identified and a grid of 100 × 100 μm was overlaid. The counting frames were set at 100 × 100 μm for DLCTX and 200 × 200 μm for HIPP stereological cell count. Investigators remained blind to the animal identity and staining antibodies throughout the study (Walker & Rosenberg, 2009).

2.4. TUNEL staining

Terminal deoxynucleotidyl transferase dUTP nick end labeling (TUNEL) staining was performed on 15 W old brain sections using TUNEL assay kit (Roche, In Situ Cell Death Detection Kit, TMR Red; Cat # 12156792910) followed by NeuN immunofluorescence labeling (see above and as previously described) (Maphis et al., 2015). Confocal images were acquired and analyzed with a Zeiss inverted Meta confocal microscope and Zeiss Zen software.

2.5. Neuroglobin and β-Amyloid$_{1-42}$ ELISAs

Microdissections of left and right hemispheres of the DLCTX and HIPP were obtained at the 15 W timepoint from SHRSP/JPD ($n = 7$) and WKY ($n = 4$) controls. One hundred mg of tissue was weighed and homogenized in 1 mL of 1 × PBS with added protease inhibitor cocktail containing AEBSF and PMSF. A tissue tearor followed by a sonicator were used for lysate preparation. The protein concentration in each sample was measured using BCA and microBCA protein assays (Thermo Fisher Scientific, Inc.).

For Ngb ELISA, samples were freeze-thawed twice and stored in −20 °C to break the cell membranes. Next, lysates were centrifuged for 5 min at 5000*g* at 4 °C. The supernatant was removed and assayed immediately. Samples were diluted 1000-fold in PBS and 100 μL of sample per well was loaded on a 96-well plate coated with rat specific Ngb antibody, according to manufacturer instructions (Cusabio Biotech, College Park, MD, USA).

For $A\beta_{1-42}$ ELISA, samples were prepared in a cold 5 M guanidine HCl/50 mM Tris·HCl (pH 8.0) solution. Homogenates were mixed for 3 h at RT and centrifuged at 16,000 *g* for 20 min at 4 °C. The supernatant was removed, 150 μL of cortical and hippocampal lysates were loaded onto a 96-well plate coated with a monoclonal antibody recognizing the NH2 terminus of mouse $A\beta_{1-42}$. Cortical samples were diluted 1:5 with standard diluent buffer, as recommended by the manufacturer (Invitrogen). A microplate reader (Multiskan, Thermo Fisher Scientific Inc.) was used to quantify AB_{1-42} at 450 nm.

2.6. NADPH oxidase activity assay

NADPH oxidase activity was determined at the 15 W timepoint, as previously described (Lu et al., 2017; Zhang et al., 2009). Briefly, 50 μg of cortical and hippocampal lysates from WKY ($n = 5$) and SHRSP/JPD ($n = 8$) were used to measure NADPH oxidase enzymatic activity based on superoxide-induced lucigenin photoemissions. The data, expressed in relative light units change per μg of protein, were collected in 5 min intervals using a luminometer (PE Applied Biosystems, Bedford, MA). The enzymatic reaction was initiated with the addition of NADPH. NADPH oxidase enzymatic activity was calculated as OD/μg protein/min.

2.7. Electron paramagnetic resonance

A lithium phthalocyanine (LiPc) electron paramagnetic resonance (EPR) oximetry probe was surgically implanted for the detection of *in*

vivo cortical O_2 levels in WKY ($n = 5$) and SHRSP/JPD ($n = 8$), as previously described (Weaver et al., 2014). Briefly, rats were anesthetized with isoflurane (4% in N_2O:O_2(70:30%) for induction and 2% in N_2O:O_2 (70:30%) for maintenance, and a pinhole was drilled into the skull at stereotaxic coordinates of the DLCTX, as determined by a Rat Brain Atlas: AP: −0.34 mm and ML: +0.4 mm right from the midline at 10 W of life. A LiPc crystal of 0.2 mm in diameter was placed at a depth of −0.25 mm using a guide microdialysis cannula. The location of the implanted LiPc crystal was initially detected by MRI and then confirmed in coronal sections postmortem. It is noteworthy that the implantation surgery has been well characterized by our group and is not associated with neuroinflammation or tissue damage (Liu et al., 1993, 2004a; Shen et al., 2009). Following a 48-h recovery period, the temporal profile of interstitial partial pressure of oxygen (pO_2) was established, with weekly readings from 10 W–15 W in experimental and control groups, based on prior reports (Liu et al., 2004a, 2004b; Shen et al., 2009). Rats were anesthetized for weekly EPR oximetry recordings and placed under a heat lamp to maintain core (rectal) body temperature of 37 °C while in the EPR cavity. An external loop resonator positioned over the LiPc implantation site provided a recording of the EPR spectrum (scan time of 40 s per scan) using a Bruker EleXsys E540 EPR spectrometer (Bruker Instruments, Billerica, MA, USA). EPR acquisition parameters were as follows: microwave power of 18 mW, a microwave frequency of 1.07 GHz, a center magnetic field strength of 380 G, a scan range of 1.0 G, and a modulation amplitude of less than a third of the intrinsic EPR linewidth (Weaver et al., 2014). Five scans were averaged to produce accurate signal-noise ratios and the peak-to-peak spectral linewidth was converted to pO_2 values using a calibration curve, as was previously documented by our collaborators (Liu et al., 2004a, 2004b; Shen et al., 2009).

2.8. Magnetic resonance imaging

2.8.1. Animal studies

Brain measurements of gray (DLCTX, HIPP) and white (CC, EC) matter structures were performed using a 4.7 T small animal MRI (Bruker, Biospin) prior to sacrifice, as previously reported (Sood et al., 2009). Animals were anesthetized with isoflurane (4% in N_2O:O_2(70:30%) for induction and 2% in N_2O:O_2 (70:30%) for maintenance. Normalized T_2-weighted intensity ratios (mean region of interest/corresponding to the *temporalis* head muscle) and brain volumes (VOL) were calculated from T_2-weighted spin-echo imaging scans (TR = 5000 ms, TE = 56 ms, pixel number = 256 × 256, FOV = 4 cm). Cerebral microbleeds were measured from acquired T_2-weighted MRI scans, as described (Greenberg et al., 2009). Diffusion tensor imaging (DTI) parameters collected and analyzed include apparent diffusion coefficient (ADC) and fractional anisotropy (FA) measuring tissue microstructural integrity through magnitude and directionality of water movement and arterial spin labeling (ASL) detecting changes in CBF.

2.8.2. Human MRI hippocampal and cortical volumetric studies

Subcortical ischemic vascular disease of the Binswanger type (SIVD-BD) is a form of VCID characterized by extensive white matter hyperintensities that has similar pathological changes in the human brain as seen in the SHRSP (Huisa & Rosenberg, 2014). The cell death in the HIPP and dorsal cortex in SHRSP suggests that hypoxia damages both

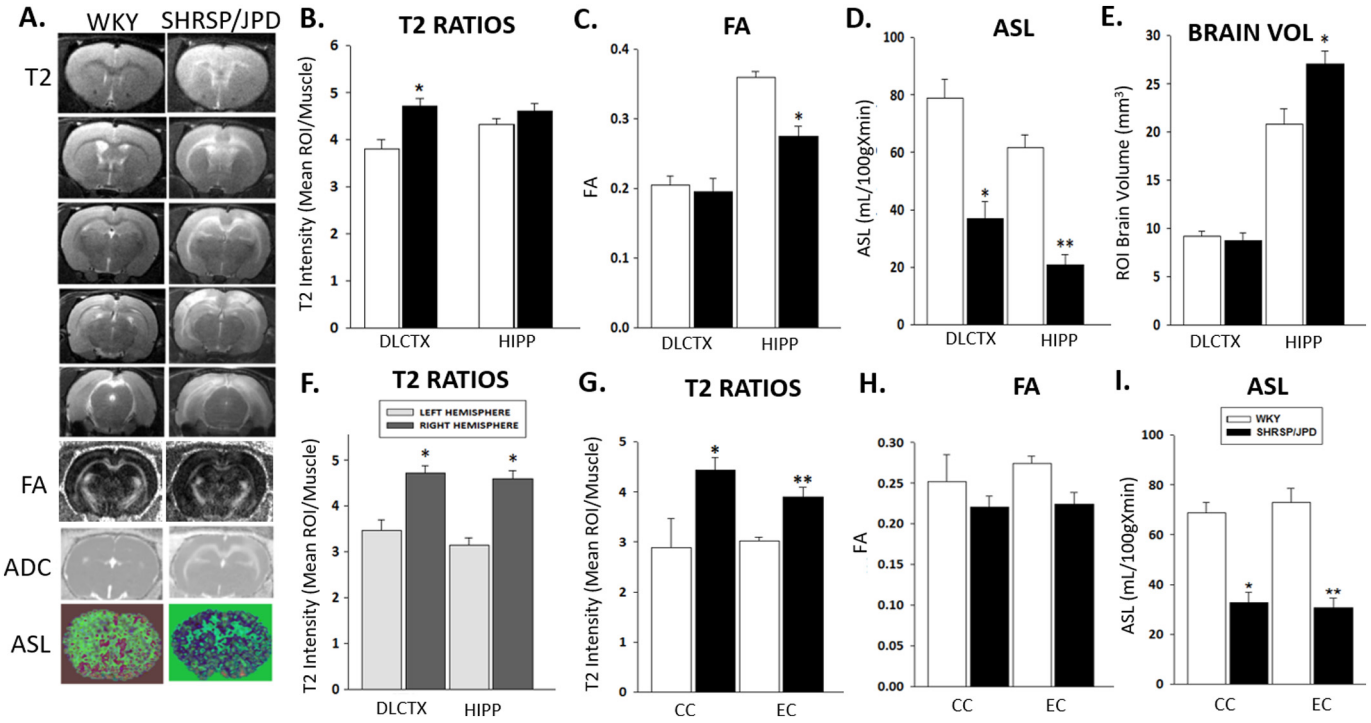

Fig. 1. Structural alterations to the GM and impaired WM tracts in the SHRSP/JPD model. (A). Representative slices of T2-MRI maps from WKY and SHRSP/JPD and corresponding quantification in the right hemisphere. (B). Regions of interest (ROI), DLCTX and HIPP, were normalized to corresponding head muscle. A significantly higher T2-intensity ratio is observed in DLCTX of SHRSP/JPD (DLCTX: $p = .018$*) compared with WKY controls. (C). Lower FA in the HIPP of SHRSP/JPD model ($p = .013$*) compared to WKY controls reflects axonal damage to WM tracts. No changes were observed between groups in the DLCTX. (D). Quantification of ASL maps shows diminished CBF in the DLCTX ($p = .005$*) and HIPP ($p < .001$**) of SHRSP/JPD model compared to controls. (E). DLCTX and HIPP ROI of total brain VOL. Hippocampal region quantification suggests elevated brain edema ($p = .040$*), which is absent from WKY controls. (F). T2-MRI intensity ratios in the DLCTX and HIPP of the SHRSP/JPD model suggest that most of the neuropathological damage occurs in the right hemisphere compared to the left in both groups (*$p < 0.001$). Data represent WKY ($n = 3$) and SHRSP/JPD ($n = 13$). (G). Quantification of CC and EC WM tracts in the right hemisphere of SHRSP/JPD model compared to controls. Increased pixel intensity T2-MRI ratios normalized to corresponding head muscle in SHRSP/JPD versus WKY controls (CC: $p = .016$*, EC: $p = .049$**). (H). No significant changes were observed in CC and EC FA measurements indicative of lack of axonal damage in these regions. (I). ASL shows a significant reduction in CBF in CC ($p = .001$*) and EC ($p < .001$**) brain ROI. Data is representative of WKY (n = 3) and SHRSP/JPD (n = 13).

the WM and GM structures. Therefore, we studied a group of patients with SIVD-BD (n = 38; mean age = 68; male/female ratio = 23/15) and compared them to healthy controls, (n = 47; mean age = 63; male/female ratio = 18/29) with MRI. All patients with cognitive impairment passed a test of competency to assure they understood the proposed studies. Control subjects were healthy elderly volunteers. A multi-echo MPRAGE sequence was used for T_1-weighted images on a Siemens 3 T scanner. The imaging parameters were field-of-view = 256 mm, image resolution = 1x1x1 mm^3, TR = 2530 ms, TE = five values, TI = 1200 ms, and an acquisition time of 6 min. The patients were a part of an on-going study of biomarkers in vascular cognitive impairment. The patients had extensive WM hyperintensities and clinical findings consistent with a diagnosis of SIVD-BD. All patients had the diagnoses based on clinical, neuropsychological, imaging and cerebrospinal fluid biomarkers collected as part of the study. Automated VOL of the right and left hippocampal volume (HV) and mean cortical thickness (mCT) for 34 cortical regions, and a mCT for the whole brain were calculated. The mCT and the HV were calculated by the FreeSurfer software program (https://surfer.nmr.mgh.harvard.edu). The total HV over the two hemispheres was normalized to the total intracranial VOL for each subject and rescaled by a constant scale factor to the mean intracranial VOL of controls. This keeps the reported unit of HV in cm^3. A mCT was taken as the average of the 34 regions combined over both hemispheres and the mean thickness was not normalized.

3. Statistics

Differences between treatment groups were analyzed using Sigma Plot (Version 12.0, Systat Software Inc., San Jose, CA, USA). Data are presented as mean ± SEM. A p-value of $< .05$ was considered statistically significant. Power calculations determined a power of $> 80\%$ with a sample size of 7 assuming an α-level of .05. One-Way ANOVA followed by a Holm-Sidak post-hoc test or an unpaired Student's t-test for two-group comparisons were used to compare experimental and control groups, where appropriate. Pairwise group differences for HV and mCT between healthy controls and each of the patient groups were calculated, incorporating age and gender as covariates. Box plots for HV and mCT were drawn to compare the SIVD-BD group to the control group of subjects. The box plots depict the standard five-number summary, which includes the minimum, first quartile, median, third quartile, and maximum, excluding the outliers (+). Multiple linear regression was done to study HV and mCT group differences between SIVD-BD and healthy control subjects with age, gender, and magnetic field strength as covariates.

4. Results

4.1. Characterization of the SHRSP/JPD model

Assessment of the SHRSP/JPD model reveals lower body weight (228.4 g, Supplemental Fig. 1A) and higher blood pressure (BP, 227 mmHg, Supplemental Fig. 1B) by 15 W as compared to age-matched WKY controls. A timecourse analysis shows a continuous reduction in weight in SHRSP/JPD (12 W: p = .009; 13 W–15 W: $p < .001$), corresponding to a significant increase in BP ($p < .001$) as compared to WKY controls. Observations prior to sacrifice indicated that 21% (3/14) of the SHRSP/JPD exhibited a seizure-like phenotype. Findings from T_2-weighted MRI indicated that 36% (5/14) of the experimental animals had microhemorrhages with average hemorrhage sizes of 1.4 mm in the DLCTX, 3 mm in the CC and 2 mm in the HIPP, while 64% (9/14) showed hyperintensities in the left and/or right hemispheres. One rat in the experimental group died during anesthesia administration for MRI measurements.

4.2. Increased brain injury in the SHRSP/JPD model

We observed structural changes in GM regions, which include DLCTX and HIPP in the SHRSP/JPD, but not in WKY control rats. The DLCTX was the cortical sub-region that showed increased injury.

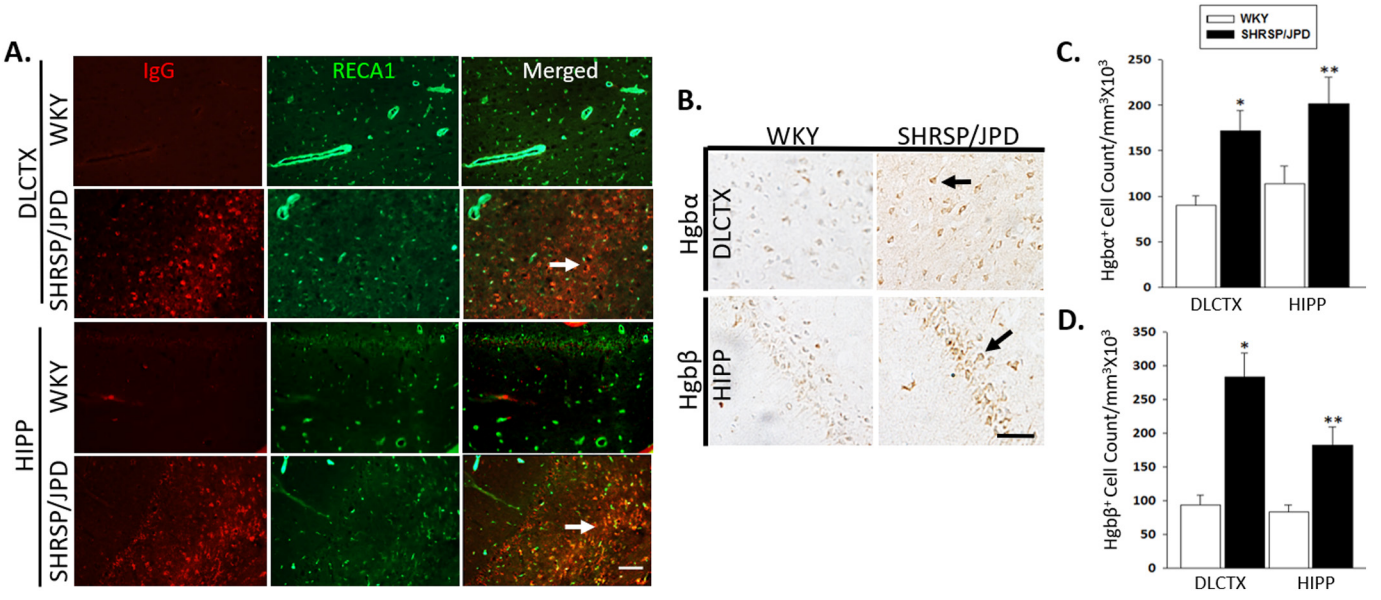

Fig. 2. Hgb leakage from the peripheral circulation occurs through an opened BBB in the SHRSP/JPD model. Red blood cell-derived Hgb from the peripheral circulation may enter the brain through a damaged BBB at 15 W timepoint. (A). Representative images of IHC triple staining for IgG (BBB leakage, red), RECA1 (endothelial cell, green) markers. Microbleeds suggest increased BBB permeability in SHRSP/JPD compared to WKY controls (merged images, arrows). Bar = 20 μm; 20× magnification. (B). Higher DAB immunoreactivity of Hgbα and Hgbβ is found in the DLCTX and HIPP of the experimental group while low expression is detected in controls. Bar = 100 μm, 20×. (C). Stereology showing a higher $Hgb\alpha^+$ cell count in the DLCTX (*p = .047) and HIPP (**p = .043) of the SHRSP/JPD model versus WKY controls. (D). Stereology showing a higher $Hgb\beta^+$ cell count in the DLCTX (*$p < .001$) and HIPP (**p = .043) of the SHRSP/JPD model. n = 4–5 rats/group. Hgb = Hemoglobin; BBB = blood brain barrier. (For interpretation of the references to colour in this figure legend, the reader is referred to the web version of this article.)

Representative MRI maps at 15 W (Fig. 1A) show greater brain injury in SHRSP/JPD, as quantified by higher normalized T2-hyperintensity ratios (DLCTX: $p = .018$, Fig. 1B), lower hippocampal FA ($p = .013$, Fig. 1C) and reduced ASL (DLCTX: $p = .005$; HIPP: $p < .001$; Fig. 1D) versus controls. Measurements of total hippocampal brain VOL in SHRSP/JPD show a significant increase ($p = .040$; Fig. 1E) as compared to WKY controls, characteristic of edema. There were significant hemispheric differences, with the right hemisphere showing higher normalized T2-hyperintensity ratios compared to the left, in both DLCTX and HIPP ($p < .001$; Fig. 1F). Therefore, we focused our neuropathological studies on the right hemisphere. Structural changes to WM tracts of the CC and EC were also detected by MRI. Results show higher normalized T2-hyperintensity ratios (CC: $p = .016$; EC: $p = .049$; Fig. 1G) and reduced CBF (CC: $p = .001$; EC: $p < .001$; Fig. 1I) in SHRSP/JPD compared with controls. No changes in FA were observed in WM brain regions of interest (Fig. 1H).

BBB permeability in the SHRSP/JPD model was determined by IHC staining for IgG (BBB leakage) and RECA1 (endothelial cell) markers. Results at 15 W demonstrate evidence for BBB leakage by the colocalization of IgG with RECA1 in the DLCTX and HIPP regions of experimental animals but not in controls (Fig. 2A). Primary antibody omissions confirmed antibody specificity in all histological experiments. Subsequent experiments were designed to determine a mechanistic link between BBB opening and the peripheral circulation.

DAB staining for cortical and hippocampal Hgbα and Hgbβ showed higher levels in the SHRSP/JPD group (Fig. 2B), which was confirmed by positive cell counts ($Hgb\alpha^+$ cells – DLCTX: $p = .047$, HIPP: $p = .043$; $Hgb\beta^+$ cells – DLCTX: $p < .001$, HIPP: p = .043) compared to low Hgb expression in controls (Fig. 2C&2D). It is noteworthy that these blood-based markers are likely derived from cerebro-microvessels and damaged tissues since all animal brains were perfused prior to histological analysis. Additional HIPP subregional differences were also found, with $Hgb\alpha^+$ (Supplemental Fig. 2C) and $Hgb\beta^+$ (Supplemental Fig. 2D) cells significantly elevated in the CA1 ($p = .048$, $p = .014$) and CA3/DG ($p = .041$, $p = .050$) SHRSP/JPD brain regions compared with age-matched WKY controls.

4.3. Hypoxic hypoperfusion contributes to brain damage

To investigate whether a state of chronic hypoxia exists in our model, we relied on a minimally invasive EPR oximetry for the study of in vivo cortical O_2 levels. A LiPc EPR probe detecting O_2 levels was surgically implanted in the right DLCTX brain region at 10 W of life in experimental and control groups. The probe location was confirmed in post-mortem tissue slices, as indicated in Fig. 3A. A timecourse of EPR recordings in live rats for interstitial pO_2 levels from 10 W–15 W was

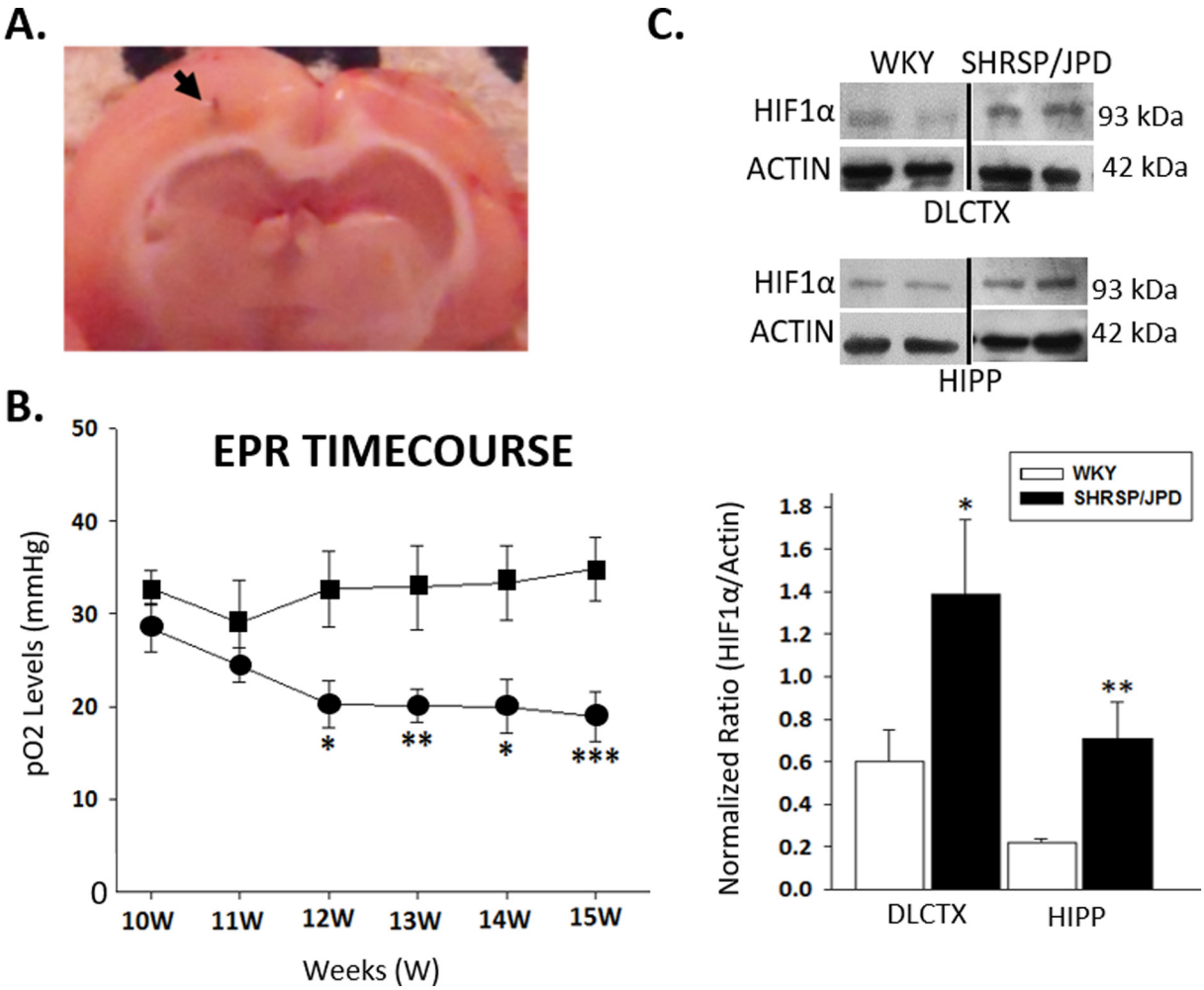

Fig. 3. Cortical and hippocampal hypoxic hypoperfusion in the SHRSP/JPD model. (A). Brain section from SHRSP/JPD confirming the Lithium Phthalocyanine crystal implantation in the right DLCTX (arrow) at 10 W of life. (B). Timecourse of EPR oximetry measurements of interstitial pO_2 readings obtained weekly from 10 W–15 W (WKY, $n = 5$, squares; SHRSP/JPD, $n = 8$, circles) demonstrates a significant drop in pO_2 levels at 12 W (*$p < .05$) which remain low until 15 W (**$p < .01$, ***$p < .001$). (C). Representative WB bands are presented for HIF1α and normalized to actin loading control. Quantification reveals elevated protein expression for HIF1α/actin ratio in the DLCTX (*$p = .05$; $n = 4$–5/group) and HIPP (**$p = .046$; $n = 3$/group) brain regions of SHRSP/JPD compared to controls. WB lanes were run on the same gel but are noncontiguous.

performed (Fig. 3B). We observed a significant drop in pO_2 of SHRSP/JPD at 12 W ($p < .05$), which remained consistently low until 15 W (13 W: $p < .01$, 14 W: $p < .05$, 15 W: $p < .001$), whereas age-matched WKY controls maintained normal pO_2 levels. Additional biochemical studies confirmed the EPR findings and demonstrated a state of hypoxic hypoperfusion in the SHRSP/JPD model. We measured HIF1α protein expression by WB, a transcriptional regulator elevated during hypoxia, and compared it to an actin loading control. Consistent with EPR data, we found HIF1α upregulation in the DLCTX ($p = .05$) and HIPP ($p = .046$), where HIF1α protein expression more than doubled in SHRSP/JPD compared to normotensive WKY controls (Fig. 3C).

After observing that hypertension-induced hypoxia occurs in the SHRSP/JPD model, we set out to determine the molecular pathways contributing to the observed brain damage. We measured free radical production at 15 W (4 W after the initiation of the high salt diet) by the activity of NADPH oxidase, a generator of superoxide and a potent free radical. Results indicate a non-significant trend for increased NADPH enzymatic activity in the DLCTX ($p = .072$), with a robust increase in NADPH oxidase ($p = .013$) in the SHRSP/JPD HIPP compared to WKY controls (Fig. 4A). Second, we determined the level of the reactive nitrogen species (RNS), 3-NT, in total DLCTX and HIPP lysates. Although a band for 3-NT DLCTX protein expression was absent (*data not shown*), we observed a significant increase in hippocampal 3-NT levels normalized to actin loading control in SHRSP/JPD compared to WKY ($p = .003$, Fig. 4B). We also stained for the lipid peroxidation marker, 4-HNE, in cortical and hippocampal brain slices (Fig. 4C). Pixel intensity quantification revealed a significant increase in 4-HNE$^+$ cells in SHRSP/JPD model but not in WKY controls (DLCTX: $p < .001$; HIPP: $p = .006$). Since we hypothesized that the O_2-carrying molecule, Ngb, may trigger downstream pathways involved in hypoxia, we conducted triple staining colocalization experiments examining Ngb, NeuN (neuronal marker) and DAPI (nuclear counterstain). The data show diminished neuronal Ngb levels in the DLCTX and HIPP regions of SHRSP/JPD compared to controls (Fig. 4D). ELISA quantification confirms these findings, showing significantly reduced hippocampal Ngb protein expression ($p = .008$) in SHRSP/JPD versus controls (Fig. 4E).

4.4. Neuropathological correlates of hypoxic injury

To investigate the neuropathological correlates of SVD in our model, experiments were designed to quantify protein misfolding and aggregation. First, we tested the profile of tau pathology using DAB staining for AT180$^+$ cells targeting mid-stage p-Tau, phosphorylated epitope site pThr231, (Fig. 5A). Stereological quantification confirmed

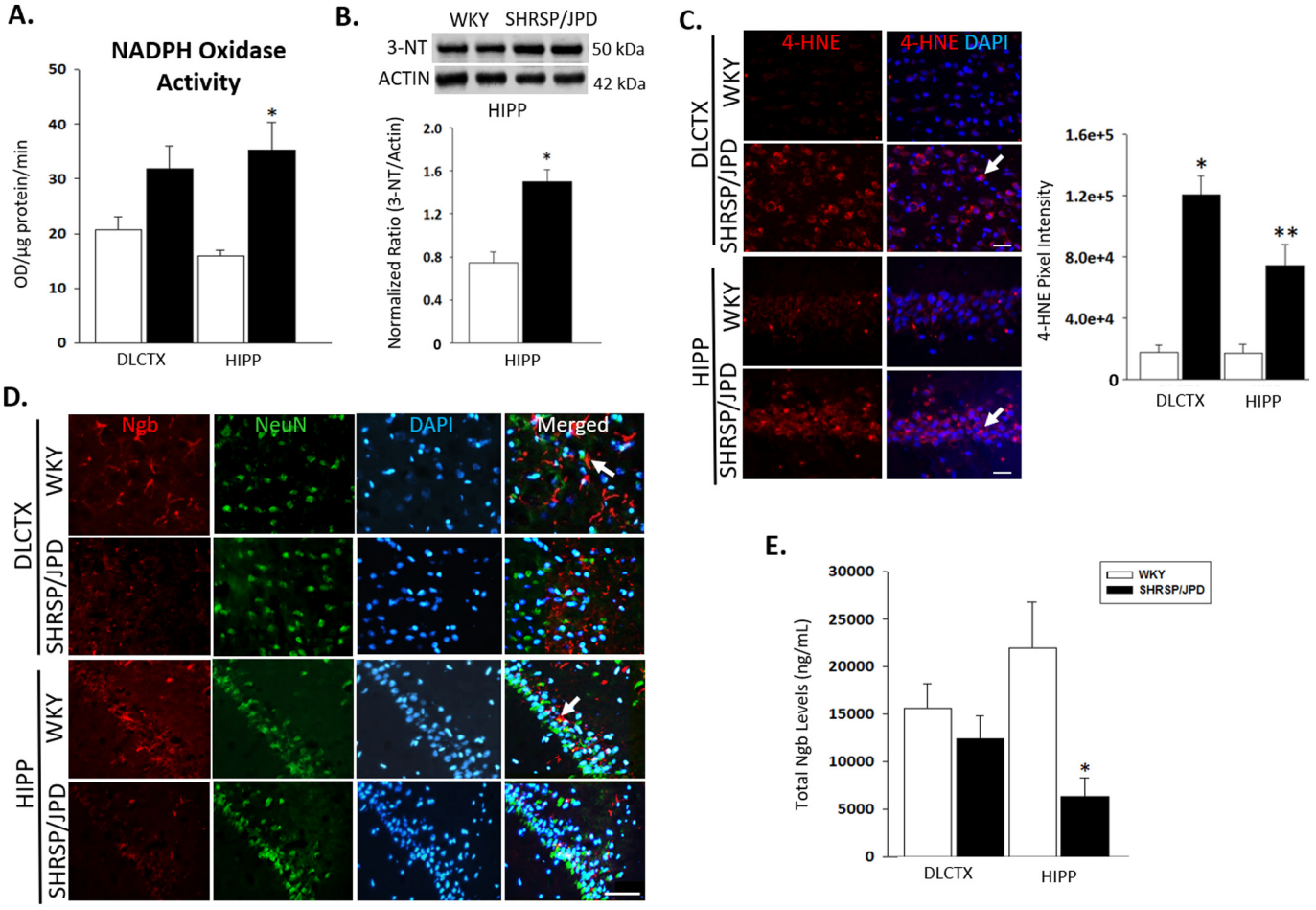

Fig. 4. Hypoxia increases free radical production and reduces Ngb levels. (A). Increased NADPH oxidase activity after 4 W of JPD diet in the DLCTX ($p = .072$, non-significant trend) and HIPP (*$p = .013$) of SHRSP/JPD model compared to age-matched controls. (B). Increased HIPP 3-NT protein expression normalized to actin loading control in total WB brain lysates of SHRSP/JPD versus WKY (*$p = .003$, $n = 4$/group). (C). Double staining for lipid peroxidation marker (4-HNE, red) with DAPI nuclear counterstain (blue) with quantification. Results show increased free-radical mediated tissue injury in the DLCTX (*$p < .001$) and HIPP (**$p = .006$) of the SHRSP/JPD model (arrows) which is absent from controls. Quantification of 4-HNE pixel intensity was measured in $n = 5$ animals/group. Bar = 55 mm, 40×. (D). Representative images of IHC triple staining in the DLCTX and HIPP. Increased colocalization (arrows) of Ngb (O_2 carrying molecule, red) with NeuN (neuronal marker, green) and DAPI (nuclear marker, blue) in WKY versus SHRSP/JPD. Bar = 10 µm, 40×. (E). ELISA quantification of total brain Ngb protein expression in the DLCTX and HIPP of experimental versus control rats. Results show diminished Ngb levels in the HIPP of SHRSP/JPD (*$p = .008$, $n = 6$–11) compared with WKY controls ($n = 4$). (For interpretation of the references to colour in this figure legend, the reader is referred to the web version of this article.)

that p-Tau is significantly higher in the DLCTX (p = .011) and HIPP (p = .003) of SHRSP/JPD compared to WKY controls (Fig. 5B). An additional p-Tau marker, ALZ50, which is a conformation-specific antibody targeted against amino acids 2–10 and 312–342 of misfolded tau and detects pre-tangle conformation of pathological tau, also appeared to be elevated in SHRSP/JPD but not in WKY controls (*data not shown*). Quantification of AT180 demonstrated a higher p-Tau normalized to total tau (Tau5) ratio, standardized against an actin loading control, in SHRSP/JPD compared to WKY rats (DLCTX: p = .010, HIPP: p = .038; Fig. 5C). Subregional differences were also detected in the HIPP, with CA1 and CA3/DG containing the highest AT180$^+$ neurons in SHRSP/JPD versus controls (CA1: p = .015; CA3/DG: p = .007, Supplemental Fig. 2A). These results were also confirmed using ALZ50 *(data not shown)*. Experiments testing for aggregates of p-Tau, as detected by Gallyas Silver impregnation, did not reveal any evidence of mature NFTs in both experimental and control groups *(data not shown)*, suggesting that the observed tau pathology may be at the pre-tangle stage at 15 W of age. Second, we studied α-synuclein (SYNUC), a protein altered and aggregated in Parkinson's disease and Lewy Body Dementia, characterized by Lewy bodies (Wong, 2017). Histological and biochemical analyses failed to show differences in α-SYNUC protein expression between experimental and control groups (Fig. 5D, E). Third, we investigated the Aβ_{1-42} peptide (targeting rat Aβ and corresponds to amino acids 33–42 of human Aβ_{1-42}) in the SHRSP/JPD model, which is recognized as a neurotoxic and aggregated Aβ known to deposit as senile plaques in AD. We observed the lack of significant differences in Aβ_{1-42} immunoreactivity (Fig. 5F) and protein levels measured by ELISA (Fig. 5G), as well as the absence of Cerebral Amyloid Angiopathy (CAA), a condition characterized by Aβ deposition along blood vessel walls, in the DLCTX and HIPP regions of experimental and control groups (Fig. 5H). In line with our hypothesis, we predicted that a pro-inflammatory cascade will be initiated by hypoxia and serve as an important mediator of neuropathological changes leading to neuronal cell death in our model. We next explored evidence for inflammation by

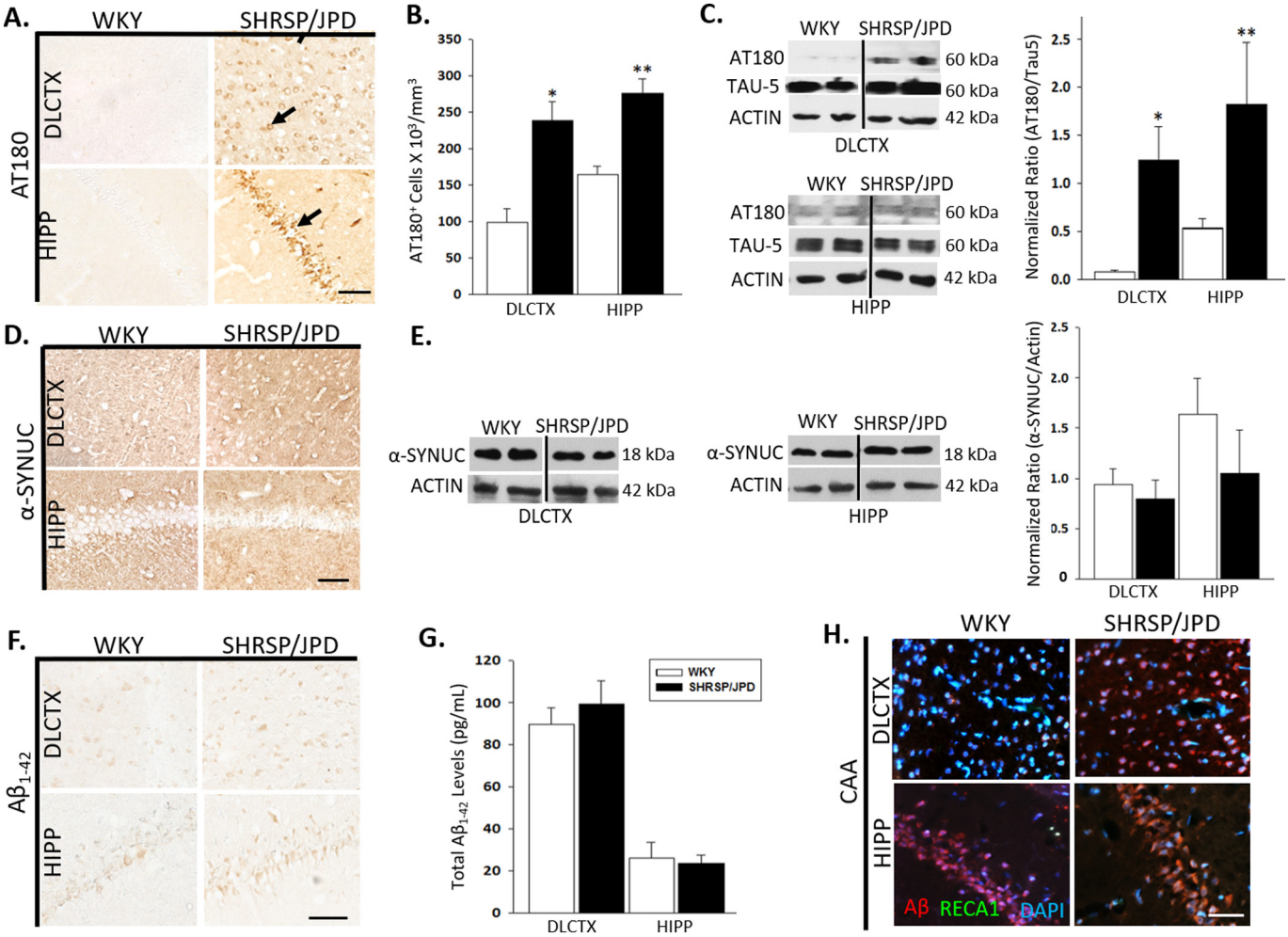

Fig. 5. Increased p-Tau but not α-SYNUC and Aβ neuropathology in the SHRSP/JPD model. (A). Representative images showing high AT180$^+$ cells (at phosphorylated epitope site pThr231 of tau) DAB staining in the DLCTX and HIPP of SHRSP/JPD absent from WKY controls with corresponding stereology quantification. Bar = 20 μm, 20×; n = 4–5/group. (B). DLCTX: *p = .011; HIPP: **p = .003. (C). WB analysis of AT180 protein expression normalized to total tau (Tau5) and actin loading control. Representative bands demonstrate higher p-Tau levels in SHRSP/JPD versus WKY age-matched controls (DLCTX: *p = .010; HIPP: **p = .038; n = 3–5/group). WB lanes were run on the same gel but are noncontiguous. (D). Representative DAB staining for α-SYNUC indicate no differences between SHRSP/JPD and WKY groups in studied ROI. Bar = 20 μm; 20× magnification, n = 4–6/group. (E). Corresponding α-SYNUC WB bands normalized to actin reveal no significant differences between experimental and control groups in the DLCTX and HIPP brain regions. α-SYNUC = alpha Synuclein, n = 3–5/group. (F). Representative DAB images for Aβ_{1-42} (corresponds to amino acids 33–42 of human Aβ_{1-42}) show unchanged immunoreactivity in experimental and control groups. Aβ = Beta-Amyloid. Bar = 10 μm; 40× magnification, n = 3–5/group. (G). ELISA quantification of total Aβ_{1-42} levels in DLCTX and HIPP brain lysates did not show significant differences between groups. n = 4–7/group. (H). Triple IHC staining for Aβ (red), RECA1 (endothelial cell marker, green) and DAPI (nuclear stain, blue) demonstrates a lack of CAA in SHRSP/JPD and WKY groups. CAA = Cerebral Amyloid Angiopathy; Bar = 10 μm; 40× magnification, n = 4/group. (For interpretation of the references to colour in this figure legend, the reader is referred to the web version of this article.)

labeling microglia with an antibody that is a specific microglial marker, CX3CR1 (fractalkine receptor) (Cardona et al., 2006). The SHRSP/JPD model showed robust CX3CR1$^+$ microglial cells in the HIPP (Fig. 6A). In contrast, microglia appeared resting with only basal immunoreactivity to CX3CR1 in WKY controls. To assess activated microglia-induced pro-inflammatory cytokine release, we measured IL-1β expression. Since IL-1β is one of the important pro-inflammatory cytokines known to promote inflammatory cascade in the brain (Wang et al., 2015) and also relevant to VCID (Brosseron et al., 2014), we focused on IL-1β. We found elevated active- IL-1β levels via WB in the HIPP of SHRSP/JPD versus controls ($p < .001$, Fig. 6B). Finally, there was clear evidence of neurodegeneration in the DLCTX and HIPP of the SHRSP/JPD model. DAB staining for NeuN (neuronal marker, Fig. 6C) and corresponding NeuN$^+$ cell counts (Fig. 6D) confirmed that neuronal cell death is occurring in SHRSP/JPD brains but not in age-matched WKY controls (DLCTX: $p = .043$, HIPP: $p = .044$). We detected HIPP subregional differences in NeuN$^+$ cell number, which were significantly reduced in the CA1 ($p = .032$) and CA3/DG ($p = .021$) of SHRSP/JPD versus WKY controls (Supplemental Fig. 2B). The presence of numerous TUNEL$^+$ cells in the HIPP suggested that the neurodegeneration is likely occurring via apoptosis (Fig. 6E).

Finally, to determine if the neuronal atrophy observed in SHRSP/JPD animal model would correlate with human VCID, we performed FreeSurfer analysis in human subjects with clinical diagnosis of Subcortical Ischemic Vascular Disease of the Binswanger type (SIVD-BD) – a type of VCID. The right and left hippocampi had similar volumes in SIVD-BD and healthy controls, justifying reported results for the total hippocampus volume (HV). Fig. 7A and B are box plots for HV and mean cortical thickness (mCT), respectively. The regression analysis showed that both HV and mCT were significantly lower in SIVD-BD group with respect to the healthy control group ($p < .05$). Age and the scanner magnetic field strength were significant factors, with older age having lower HV and mCT and higher magnetic field strength giving higher values for HV and mCT. Gender was significant for HV but not for mCT, with females having a higher normalized hippocampal volume. Altogether, these results corroborated with our pre-clinical animal model studies suggesting that SHRSP/JPD truly mimics neurodegenerative aspect of SIVD-BD (a type of VCID).

5. Discussion

Our results suggest that hypoxic hypoperfusion initiates a neuropathological cascade involving free radical production, microglial activation, BBB disruption and tau hyperphosphorylation in the GM of SHRSP/JPD (Fig. 8). Earlier studies showed that chronic hypoxia induced by permanent unilateral carotid artery occlusion and followed by a 4 W high salt diet is sufficient to induce long-term neuropathological and vascular WM changes consisting of neuroinflammation, BBB dysfunction, brain injury and cognitive impairment in the SHRSP/JPD model (Jalal et al., 2012, 2015; Weaver et al., 2014). The present study extends these findings to the DLCTX and HIPP GM in a non-occluded rat model, thereby linking hypoxia and cerebrovascular dysfunction with the spontaneous occurrence of tau pathology in SHRSP/JPD. Hypoxia may also exert direct effects on microglia and other supporting cells of the brain, which was omitted from Fig. 8 as studies exploring these cell types are beyond the scope of the present study.

Our findings in the accelerated SHRSP model show that a chronic state of hypoxic hypoperfusion, beginning one week following the initiation of a high salt, low protein diet, induces a global injury pattern in GM (DLCTX, HIPP) and WM (CC, EC), which is associated with a reduction in CBF to these brain regions. Changes in blood vessel morphology in SHRSP without JPD may also occur early in life (Bailey et al., 2014). Our observations are consistent with prior studies by our group showing reduced tissue pO_2 and increased HIF1α in WM of

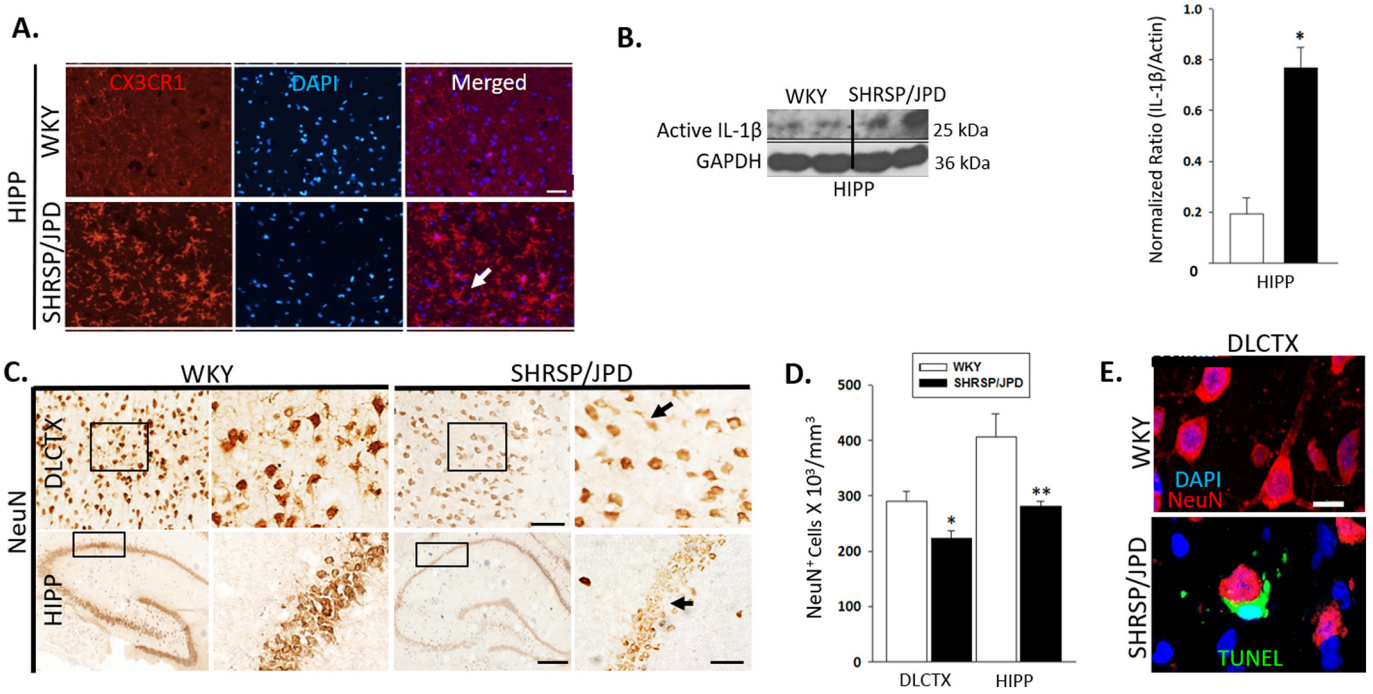

Fig. 6. Pro-inflammatory cytokine release and increased neurodegeneration in the GM of the SHRSP/JPD model. (A). IHC double staining showing robust CX3CR1$^+$ microglial activation (red) in the HIPP region colocalized with DAPI nuclear staining (blue) of SHRSP/JPD but not in age-matched controls (arrow); Bar = 20 μm, 40×. (B). WB quantification showing elevated active- IL-1β levels in hippocampal lysates of SHRSP/JPD compared with controls ($p < .001$, WKY: $n = 5$; SHRSP/JPD: $n = 7$). (C). Presence of NeuN$^+$ DAB immunoreactivity in the DLCTX and HIPP regions is significantly diminished in SHRSP/JPD compared to age-matched WKY controls. Bar = 20 μm representative of 20× and 40× magnification (black boxes represent 40× insert); HIPP 4× view, bar = 100 μm and 40× view, bar = 10 μm; $n = 5$/group. (D). Stereology quantification of NeuN$^+$ DAB staining shows reduced NeuN$^+$ cell counts in SHRSP/JPD DLCTX (*$p = .043$) and HIPP (**$p = .044$) compared to WKY; $n = 4$–5/group. (E). Presence of cortical apoptotic neurons (TUNEL$^+$ (green) and NeuN$^+$ (red)) in SHRSP/JPD ($n = 1$) absent from WKY controls ($n = 1$). Bar = 10 μm. (For interpretation of the references to colour in this figure legend, the reader is referred to the web version of this article.)

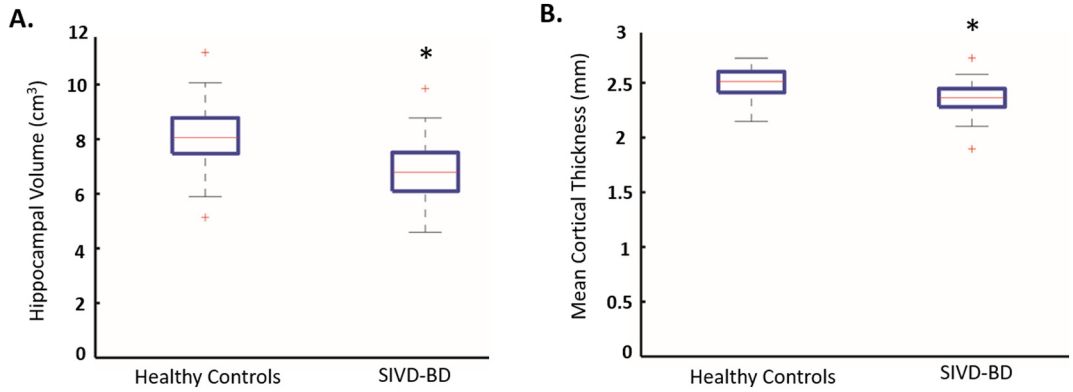

Fig. 7. Decreased hippocampal volume and cortical thickness in SIVD-BD patients. The normalized hippocampal volume (A) and the cortical thickness (B) were significantly lower in subcortical ischemic vascular disease of the Binswanger type (SIVD-BD) as compared to healthy controls (*$p < .05$) after correcting for age, gender and scanner magnetic field strength effects. Outliers are represented by a (+) symbol.

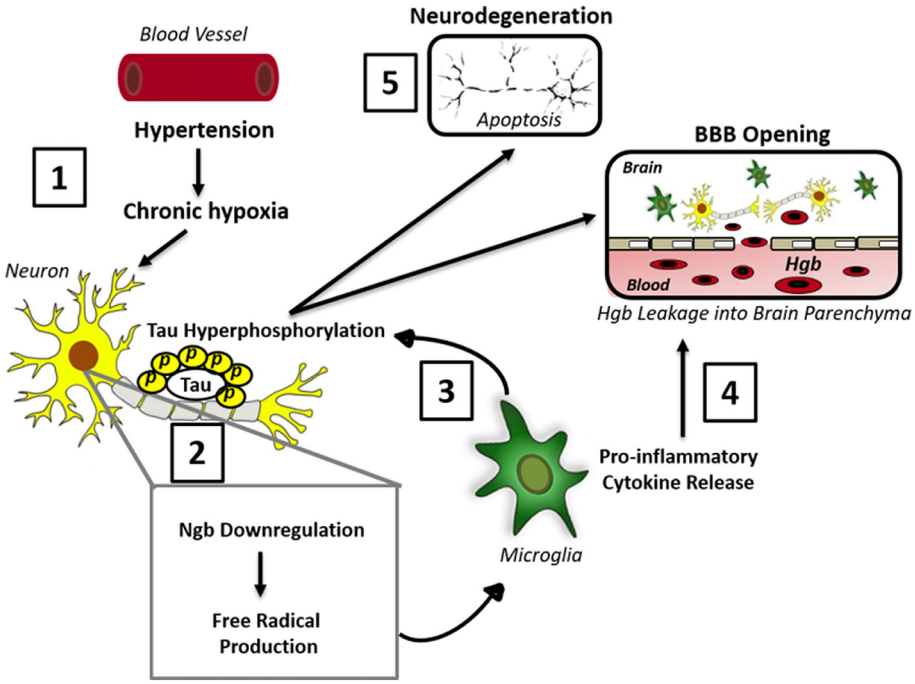

Fig. 8. Proposed working model for neuropathological change in SHRSP/JPD. We postulate that hypertension-induced hypoxia caused by changes in blood vessel morphology (1) promotes Ngb downregulation and free radical generation in neurons (2). Microglia activation and the release of pro-inflammatory cytokines ensues, thus damaging neuronal axons and triggering p-Tau (3) which may lead to Hgb leakage from the periphery through damaged microvasculature of the BBB (4) and apoptotic neuronal cell death (5). Neurotoxic cytokine release from active microglia may also directly promote BBB permeability. Ngb = neuroglobin, p = phosphorylation, BBB = blood brain barrier, Hgb = hemoglobin.

unilateral carotid artery occlusion subjected SHRSP (Jalal et al., 2015; Weaver et al., 2014). Low O_2 levels in the present study corresponded with increased ROS and RNS and resulted in further tissue damage. Evidence from other chronic hypoperfusion studies supports our claims, showing corresponding ROS (Pedro-Botet et al., 1992) and RNS elevation (Aliev et al., 2014) and lipid peroxidation (Montine et al., 2002), possibly suggestive of altered mitochondrial oxidative stress pathways in hypertensive rats, which may cause increased sensitivity to hypoxic insult (Ritz et al., 2012). Previously, we showed that intact mitochondrial function is essential for hippocampal neuroprotection in a 4-vessel occlusion rat model of global cerebral ischemia (Zhang et al., 2009). Therefore, we postulate that Ngb downregulation by HIF1α may trigger electron transport chain disruption in the neuronal mitochondria and the generation of O_2 and nitrogen free radicals, thus activating microglia-derived neuroinflammatory factors, including p38 mitogen-activated protein kinase (p38 MAPK), which can phosphorylate neuronal tau (Maphis et al., 2016) and promote neurodegeneration. In spite of controversial evidence surrounding Ngb expression in neurological disease (Haines et al., 2012; Ord et al., 2013), we postulate that hypertension-induced hypoxia will promote neuronal-intrinsic downregulation of Ngb as a compensatory and situation-specific physiological mechanism necessary to achieve sufficient O_2 levels. Furthermore, the link between microglia-mediated inflammation (via IL-1β), neurotoxicity and tau hyperphosphorylation/aggregation has been previously described by our group (Bhaskar et al., 2010; Maphis et al., 2015, 2016).

More relevant to the link between hypertension and tau-associated cell death, we found the hyperphosphorylation of tau in the DLCTX and HIPP of the SHRSP/JPD model, which was absent from normotensive and age-matched WKY controls. Our results are in agreement with animal studies showing p-Tau in the SHRSP CTX (Schreiber et al., 2014) and with clinical MRI studies demonstrating an association between higher Braak NFT stage and hippocampal brain atrophy (Josephs et al., 2017). We performed Gallyas silver staining but failed to detect any mature pathological tau assemblies in the studied brain regions. Therefore, we believe that some kind of soluble but toxic forms of tau oligomers or smaller aggregates may be responsible for neuronal cell death (Lasagna-Reeves et al., 2012), such as cis p-Tau, disrupting microtubule networks and propagating to nearby neurons (Kondo et al., 2015). In our studies, p-Tau correlated with significantly elevated systolic BP, which may alter microtubule motor proteins and contribute to axonal transport defects and damage to GM structures (Petrovitch et al.,

2000; Stieber et al., 1998). We did not find expression of aggregated and toxic proteins, such as Aβ and α-SYNUC. We also did not observe the presence of CAA in the SHRSP/JPD (Schreiber et al., 2012). These negative findings suggest that the observed neuropathology in our model is tau-specific (Kovacs et al., 2013).

Chronic hypertension and neurovascular dysfunction are known potential triggers for inflammation (Sochocka et al., 2013), and hypoxia-induced inflammation has been shown to promote GM damage and neurological deficits (Choi et al., 2015; Davies et al., 2013; Sironi et al., 2001, 2004). We found that hypertension-mediated hypoxia is associated with a pro-inflammatory response, BBB leakage and neurodegeneration in cortical and hippocampal brain regions of the SHRSP/JPD model. Although the precise sequence of events remains to be delineated, data from SHRSP studies suggests that free radical production promotes remodeling of the cerebrovasculature, initiating an inflammatory response and resulting in BBB permeability in GM structures (Montagne et al., 2015; Pires et al., 2013; Ueno et al., 2004). Furthermore, we speculate that neurodegeneration may likely be exacerbated by a microglia-mediated pro-inflammatory response. An increase in cytokine production was documented in the HIPP of a SHR model of VCID (Tayebati et al., 2016), which parallels our findings of elevated IL-1β expression. Our studies in SHRSP demonstrate neuroinflammation-induced vascular alterations leading to MRI injury and BBB dysfunction. One possible mechanistic explanation for a damaged BBB and Hgb leakage from the peripheral circulation into the brain parenchyma may be due to hypertension-induced transendothelial transport. Another possible explanation is a state of capillary and arteriolar erythrocyte accumulation (stases), correlating with small vessel microbleeds observed on MRI (Mencl et al., 2013; Schreiber et al., 2012). In fact, Hgb and its degradation products have been recognized as neurotoxins (Huang et al., 2006), interfering with the NADPH system and promoting lipid peroxidation (Robinson et al., 2009) in an animal model of VCID. Additionally, neuronally-derived Hgb may also contribute to the observed increase in Hgbα and Hgbβ (Ohyagi et al., 1994). Consistent with these findings, we also observed neurodegeneration in the DLCTX and HIPP regions of our SHRSP/JPD model, corresponding to higher cortical T2-hyperintensity ratios and reduced hippocampal FA as compared to normotensive WKY controls. Our observations that higher numbers of neuropathological markers accumulated in the right hemisphere compared with the left is suggestive of right hemispheric dominance and brain asymmetry in the rat circulatory system (Yamori et al., 1976; Zhang et al., 2015). Our data also revealed a higher hippocampal brain VOL in SHRSP/JPD, suggestive of vasogenic edema, as noted by Sironi and his group (Guerrini et al., 2002). Prior studies by our lab showed structural changes to the WM tracts in the CC and EC of an ischemic SHRSP model (Jalal et al., 2012). Here, we extend these findings by showing significantly higher T2-hyperintensity normalized ratios in the DLCTX, CC and EC, correlating with reduced CBF and neuronal cell death occurring by apoptosis in the accelerated SHRSP/JPD model but not in WKY rats. This is consistent with reports in SHR showing decreased neuronal cell count associated with apoptosis (Mignini et al., 2004).

The MRI findings in patients with SIVD-BD, which has similar pathological changes in the WM, showed reduced hippocampal VOL and mean cortical area. This clinical data is consistent with our findings in the animal model of neuronal cell death in the HIPP and CTX brain regions, but not with the observed increase in hippocampal VOL on MRI in the SHRSP. We propose that the rapid evolution of hypertensive damage in the SHRSP leads to an increase in vasogenic edema in the GM, which spreads to the WM (Fredriksson et al., 1985). Since there is an acceleration of the injury with dietary modification in the SHRSP, it is unlikely that there was sufficient time for the edema in the HIPP to resolve, and that over a longer timecourse, atrophy would have occurred as indicated by the cell death. Due to the rapid course of the SHRSP/JPD model, long term studies were impossible as the animals did not survive past the 16th week of life. The chronic hypoxia in human brains produced cell death with hippocampal and cortical shrinkage.

A detailed stereological study of hippocampal subregions revealed that CA1 and CA3/DG are most vulnerable to injury in the SHRSP/JPD model. We observed elevated p-Tau (AT180), Hgbα/Hgbβ and reduced $NeuN^+$ cell counts in the CA1 and CA3/DG subregions of SHRSP/JPD compared to normotensive WKY controls. Our findings are supported by studies of patients with SVD showing a distinct loss of CA1 pyramidal cells (Kril et al., 2002; West et al., 1994) and animal studies showing the effects of hypoxia on the microcirculation, leading to decreased CA1 and DG hippocampal VOL due to neuronal cell death-mediated brain atrophy (De Jong et al., 1999; Sabbatini et al., 2000, 2002). The observed increase in hippocampal brain VOL in the SHRSP/JPD model reflects brain edema which contributes to hippocampal neurodegeneration. No significant changes among groups were noted in the CA2 subregion, suggesting that this population of pyramidal neurons is physiologically distinct and resistant to hypoxic insult due to a higher action potential threshold and greater synaptic stability (Zhao et al., 2007). MRI studies in patients with SIVD-BD showed reduced hippocampal VOL and smaller cortical thickness. Since there was cell death in the hippocampal subfields of the SHRSP/JPD model and the animals died within one month after starting the diet, we speculate that had they lived longer, there would have been a noticeable loss of hippocampal and cortical brain VOL in the animals, secondary to cell death.

Our findings should be interpreted with several limitations in mind. First, our data represents a single timepoint at 15 W of life and does not capture the full spatiotemporal profile of GM and WM injury. Second, the use of an anesthetic during the MRI and EPR recordings temporarily reduces blood pressure and may alter brain neuropathology. Third, our results in the SHRSP/JPD model may not be generalizable to the entire population, in part, due to the complexity and multifactorial nature of SVD in SIVD-BD. It is important to note that there is no single animal model that truly mimics all neuropathological aspects of the disease.

6. Conclusions

In conclusion, our results suggest that hypertensive SVD lowers the threshold for injury due to cerebral hypoxic hypoperfusion. Sustained vascular dysfunction coupled with a neuroinflammatory response are sufficient to drive sporadic tau hyperphosphorylation and neurodegeneration by a hypoxia-dependent mechanism. While the observations presented in this study are correlational, they will inform future studies to explore the molecular mechanisms responsible for VCID.

Declarations

Ethics approval and consent to participate

The animal protocol was approved by the University of New Mexico Health Sciences Center Institutional Animal Care and Use Committee (IACUC), adhering to the Humane Care and Use of Laboratory Animals Policy by NIH. Studies of the patients with cognitive impairment were approved by the University of New Mexico Human Research Committee (ARFprotocol #: 15-200248-HSC; grant # related to protocol: 2 RO1 NS045847-071A). All participants have consented to participate in the study.

Consent for publication

Consent to publish individual patient data was obtained from all study participants. All authors have agreed to the submission of the manuscript.

Availability of data and materials

The datasets used and analyzed during the current study are available from the corresponding author upon reasonable request. All data generated and analyzed during this study are included in this published article and supplementary figures.

Competing interests

The authors declared that no financial and non-financial conflict of interest exists.

Funding

This study is supported by NIH/NINDS R01 NS045847-07A1 and R01 NS083704.

Authors' contributions

L.R. was responsible for the design and conceptualization of the study, analysis and interpretation of the data and drafting the manuscript. K.B. contributed to the design and conceptualization of the study, interpretation of data and revising the manuscript. J.W. collected and interpreted the EPR data. S.M. helped with the collection of the behavior data and MRI data analysis. Q.Z. was responsible for the collection, analysis and interpretation of the free radical data. J.T. helped with animal handling, collection of BP, weight data, manuscript revisions and interpretation. C.E. and S.I. contributed to the data collection, analysis and drafting of the manuscript. N.M. and L.W. collected, analyzed and interpreted the cytokine data. L.S. designed and conceptualized the study, helped interpret and troubleshoot the MRI data and revised the manuscript. A.C. contributed to the analysis of the FreeSurfer MRI human data for hippocampal and cortical volumes. J.P. and E.E. performed the statistical analysis of the human MRI data. G.R. secured funding for this study, helped with the design and conceptualization, interpretation of data and revising of the manuscript. All authors read and approved the final draft of the manuscript.

Acknowledgements

The authors would like to thank the students in the lab: Anna Diaz and Carolyn Nighbert for their technical help with experiments. We also thank Yirong Yang, PhD for acquiring the MRI of our rats and to Jim Liu, PhD for his expert guidance in the interpretation of the EPR oximetry and free radical data. Finally, we extend our gratitude to Fakhreya Jalal, PhD for establishing the high salt rat models in the lab, on which this research project is based.

Appendix A. Supplementary data

Supplementary data to this article can be found online at https://doi.org/10.1016/j.nbd.2018.07.009.

References

Aliev, G., Priyadarshini, M., Reddy, V.P., Grieg, N.H., Kaminsky, Y., Cacabelos, R., Ashraf, G.M., Jabir, N.R., Kamal, M.A., Nikolenko, V.N., et al., 2014. Oxidative stress mediated mitochondrial and vascular lesions as markers in the pathogenesis of Alzheimer disease. Curr. Med. Chem. 21, 2208–2217.

Bailey, E.L., McBride, M.W., Beattie, W., McClure, J.D., Graham, D., Dominiczak, A.F., Sudlow, C.L., Smith, C., Wardlaw, J.M., 2014. Differential gene expression in multiple neurological, inflammatory and connective tissue pathways in a spontaneous model of human small vessel stroke. Neuropathol. Appl. Neurobiol. 40, 855–872.

Bhaskar, K., Konerth, M., Kokiko-Cochran, O.N., Cardona, A., Ransohoff, R.M., Lamb, B.T., 2010. Regulation of tau pathology by the microglial fractalkine receptor. Neuron 68, 19–31.

Brittain, T., Skommer, J., Raychaudhuri, S., Birch, N., 2010. An antiapoptotic neuroprotective role for neuroglobin. Int. J. Mol. Sci. 11, 2306–2321.

Brosseron, F., Krauthausen, M., Kummer, M., Heneka, M.T., 2014. Body fluid cytokine levels in mild cognitive impairment and Alzheimer's disease: a comparative overview. Mol. Neurobiol. 50, 534–544.

Burmester, T., Hankeln, T., 2009. What is the function of neuroglobin? J. Exp. Biol. 212, 1423–1428.

Cardona, A.E., Pioro, E.P., Sasse, M.E., Kostenko, V., Cardona, S.M., Dijkstra, I.M., Huang, D., Kidd, G., Dombrowski, S., Dutta, R., et al., 2006. Control of microglial neurotoxicity by the fractalkine receptor. Nat. Neurosci. 9, 917–924.

Choi, J.Y., Cui, Y., Kim, B.G., 2015. Interaction between hypertension and cerebral hypoperfusion in the development of cognitive dysfunction and white matter pathology in rats. Neuroscience 303, 115–125.

Davies, A.L., Desai, R.A., Bloomfield, P.S., McIntosh, P.R., Chapple, K.J., Linington, C., Fairless, R., Diem, R., Kasti, M., Murphy, M.P., Smith, K.J., 2013. Neurological deficits caused by tissue hypoxia in neuroinflammatory disease. Ann. Neurol. 74, 815–825.

De Jong, G.I., Farkas, E., Stienstra, C.M., Plass, J.R., Keijser, J.N., de la Torre, J.C., Luiten, P.G., 1999. Cerebral hypoperfusion yields capillary damage in the hippocampal CA1 area that correlates with spatial memory impairment. Neuroscience 91, 203–210.

Fotuhi, M., Hachinski, V., Whitehouse, P.J., 2009. Changing perspectives regarding late-life dementia. Nat. Rev. Neurol. 5, 649–658.

Fredriksson, K., Auer, R.N., Kalimo, H., Nordborg, C., Olsson, Y., Johansson, B.B., 1985. Cerebrovascular lesions in stroke-prone spontaneously hypertensive rats. Acta Neuropathol. 68, 284–294.

Gao, L., Tian, S., Gao, H., Xu, Y., 2013. Hypoxia increases Abeta-induced tau phosphorylation by calpain and promotes behavioral consequences in AD transgenic mice. J. Mol. Neurosci.: MN 51, 138–147.

Gendron, T.F., Petrucelli, L., 2009. The role of tau in neurodegeneration. Mol. Neurodegener. 4, 13.

Gorelick, P.B., Scuteri, A., Black, S.E., Decarli, C., Greenberg, S.M., Iadecola, C., Launer, L.J., Laurent, S., Lopez, O.L., Nyenhuis, D., et al., 2011. Vascular contributions to cognitive impairment and dementia: a statement for healthcare professionals from the American Heart Association/American Stroke Association. Stroke 42, 2672–2713.

Greenberg, S.M., Vernooij, M.W., Cordonnier, C., Viswanathan, A., Al-Shahi Salman, R., Warach, S., Launer, L.J., Van Buchem, M.A., Breteler, M.M., Microbleed Study Group, 2009. Cerebral microbleeds: a guide to detection and interpretation. Lancet Neurol. 8, 165–174.

Guerrini, U., Sironi, L., Tremoli, E., Cimino, M., Pollo, B., Calvio, A.M., Paoletti, R., Asdente, M., 2002. New insights into brain damage in stroke-prone rats: a nuclear magnetic imaging study. Stroke 33, 825–830.

Haines, B., Demaria, M., Mao, X., Xie, L., Campisi, J., Jin, K., Greenberg, D.A., 2012. Hypoxia-inducible factor-1 and neuroglobin expression. Neurosci. Lett. 514, 137–140.

Henning, E.C., Warach, S., Spatz, M., 2010. Hypertension-induced vascular remodeling contributes to reduced cerebral perfusion and the development of spontaneous stroke in aged SHRSP rats. J. Cereb. Blood Flow Metab.: Official J. Int. Soc. Cereb. Blood Flow Metab. 30, 827–836.

Huang, Y., Wu, L., Xu, C., Yang, B., Wang, R., 2006. Increased HO-1 expression and decreased iNOS expression in the hippocampus from adult spontaneously hypertensive rats. Cell Biochem. Biophys. 46, 35–42.

Huisa, B.N., Rosenberg, G.A., 2014. Binswanger's disease: toward a diagnosis agreement and therapeutic approach. Expert. Rev. Neurother. 14, 1203–1213.

Humpel, C., 2011. Chronic mild cerebrovascular dysfunction as a cause for Alzheimer's disease? Exp. Gerontol. 46, 225–232.

Iadecola, C., Davisson, R.L., 2008. Hypertension and cerebrovascular dysfunction. Cell Metab. 7, 476–484.

Jalal, F.Y., Yang, Y., Thompson, J., Lopez, A.C., Rosenberg, G.A., 2012. Myelin loss associated with neuroinflammation in hypertensive rats. Stroke 43, 1115–1122.

Jalal, F.Y., Yang, Y., Thompson, J.F., Roitbak, T., Rosenberg, G.A., 2015. Hypoxia-induced neuroinflammatory white-matter injury reduced by minocycline in SHR/SP. J. Cereb. Blood Flow Metab.: Official J. Int. Soc. Cereb. Blood Flow Metab. 35, 1145–1153.

Josephs, K.A., Murray, M.E., Tosakulwong, N., Whitwell, J.L., Knopman, D.S., Machulda, M.M., Weigand, S.D., Boeve, B.F., Kantarci, K., Petrucelli, L., et al., 2017. Tau aggregation influences cognition and hippocampal atrophy in the absence of beta-amyloid: a clinico-imaging-pathological study of primary age-related tauopathy (PART). Acta Neuropathol. 133, 705–715.

Kondo, A., Shahpasand, K., Mannix, R., Qiu, J., Moncaster, J., Chen, C.H., Yao, Y., Lin, Y.M., Driver, J.A., Sun, Y., et al., 2015. Antibody against early driver of neurodegeneration cis P-tau blocks brain injury and tauopathy. Nature 523, 431–436.

Kovacs, G.G., Milenkovic, I., Wohrer, A., Hoftberger, R., Gelpi, E., Haberler, C., Honigschnabl, S., Reiner-Concin, A., Heinzl, H., Jungwirth, S., et al., 2013. Non-Alzheimer neurodegenerative pathologies and their combinations are more frequent than commonly believed in the elderly brain: a community-based autopsy series. Acta Neuropathol. 126, 365–384.

Kovari, E., Herrmann, F.R., Hof, P.R., Bouras, C., 2013. The relationship between cerebral amyloid angiopathy and cortical microinfarcts in brain ageing and Alzheimer's disease. Neuropathol. Appl. Neurobiol. 39, 498–509.

Kril, J.J., Patel, S., Harding, A.J., Halliday, G.M., 2002. Patients with vascular dementia due to microvascular pathology have significant hippocampal neuronal loss. J. Neurol. Neurosurg. Psychiatry 72, 747–751.

Lasagna-Reeves, C.A., Castillo-Carranza, D.L., Sengupta, U., Guerrero-Munoz, M.J., Kiritoshi, T., Neugebauer, V., Jackson, G.R., Kayed, R., 2012. Alzheimer brain-derived tau oligomers propagate pathology from endogenous tau. Sci. Rep. 2, 700.

Liu, K.J., Gast, P., Moussavi, M., Norby, S.W., Vahidi, N., Walczak, T., Wu, M., Swartz, H.M., 1993. Lithium phthalocyanine: a probe for electron paramagnetic resonance oximetry in viable biological systems. Proc. Natl. Acad. Sci. U. S. A. 90, 5438–5442.

Liu, S., Timmins, G.S., Shi, H., Gasparovic, C.M., Liu, K.J., 2004a. Application of in vivo

EPR in brain research: monitoring tissue oxygenation, blood flow, and oxidative stress. NMR Biomed. 17, 327–334.
Liu, S., Shi, H., Liu, W., Furuichi, T., Timmins, G.S., Liu, K.J., 2004b. Interstitial pO2 in ischemic penumbra and core are differentially affected following transient focal cerebral ischemia in rats. J. Cereb. Blood Flow Metab.: Official J. Int. Soc. Cereb. Blood Flow Metab. 24, 343–349.
Lu, Y., Wang, R., Dong, Y., Tucker, D., Zhao, N., Ahmed, M.E., Zhu, L., Liu, T.C., Cohen, R.M., Zhang, Q., 2017. Low-level laser therapy for beta amyloid toxicity in rat hippocampus. Neurobiol. Aging 49, 165–182.
Maphis, N., Xu, G., Kokiko-Cochran, O.N., Cardona, A.E., Ransohoff, R.M., Lamb, B.T., Bhaskar, K., 2015. Loss of tau rescues inflammation-mediated neurodegeneration. Front. Neurosci. 9, 196.
Maphis, N., Jiang, S., Xu, G., Kokiko-Cochran, O.N., Roy, S.M., Van Eldik, L.J., Watterson, D.M., Lamb, B.T., Bhaskar, K., 2016. Selective suppression of the alpha isoform of p38 MAPK rescues late-stage tau pathology. Alzheimers Res. Ther. 8, 54.
Mencl, S., Garz, C., Niklass, S., Braun, H., Gob, E., Homola, G., Heinze, H.J., Reymann, K.G., Kleinschnitz, C., Schreiber, S., 2013. Early microvascular dysfunction in cerebral small vessel disease is not detectable on 3.0 Tesla magnetic resonance imaging: a longitudinal study in spontaneously hypertensive stroke-prone rats. Exp. Transl. Stroke Med. 5, 8.
Mignini, F., Vitaioli, L., Sabbatini, M., Tomassoni, D., Amenta, F., 2004. The cerebral cortex of spontaneously hypertensive rats: a quantitative microanatomical study. Clin. Exp. Hypertens. 26, 287–303.
Montagne, A., Barnes, S.R., Sweeney, M.D., Halliday, M.R., Sagare, A.P., Zhao, Z., Toga, A.W., Jacobs, R.E., Liu, C.Y., Amezcua, L., et al., 2015. Blood-brain barrier breakdown in the aging human hippocampus. Neuron 85, 296–302.
Montine, T.J., Neely, M.D., Quinn, J.F., Beal, M.F., Markesbery, W.R., Roberts, L.J., Morrow, J.D., 2002. Lipid peroxidation in aging brain and Alzheimer's disease. Free Radic. Biol. Med. 33, 620–626.
Ohyagi, Y., Yamada, T., Goto, I., 1994. Hemoglobin as a novel protein developmentally regulated in neurons. Brain Res. 635, 323–327.
Ord, E.N., Shirley, R., McClure, J.D., McCabe, C., Kremer, E.J., Macrae, I.M., Work, L.M., 2013. Combined antiapoptotic and antioxidant approach to acute neuroprotection for stroke in hypertensive rats. J. Cereb. Blood Flow Metab.: Official J. Int. Soc. Cereb. Blood Flow Metab. 33, 1215–1224.
Paul, J., Strickland, S., Melchor, J.P., 2007. Fibrin deposition accelerates neurovascular damage and neuroinflammation in mouse models of Alzheimer's disease. J. Exp. Med. 204, 1999–2008.
Pedro-Botet, J., Senti, M., Nogues, X., Rubies-Prat, J., Roquer, J., D'Olhaberriague, L., Olive, J., 1992. Lipoprotein and apolipoprotein profile in men with ischemic stroke. Role of lipoprotein(a), triglyceride-rich lipoproteins, and apolipoprotein E polymorphism. Stroke 23, 1556–1562.
Petrovitch, H., White, L.R., Izmirilian, G., Ross, G.W., Havlik, R.J., Markesbery, W., Nelson, J., Davis, D.G., Hardman, J., Foley, D.J., Launer, L.J., 2000. Midlife blood pressure and neuritic plaques, neurofibrillary tangles, and brain weight at death: the HAAS. Honolulu-Asia aging Study. Neurobiol. Aging 21, 57–62.
Pires, P.W., Dams Ramos, C.M., Matin, N., Dorrance, A.M., 2013. The effects of hypertension on the cerebral circulation. Am. J. Phys. Heart Circ. Phys. 304, H1598–H1614.
Ritz, M.F., Grond-Ginsbach, C., Engelter, S., Lyrer, P., 2012. Gene expression suggests spontaneously hypertensive rats may have altered metabolism and reduced hypoxic tolerance. Curr. Neurovasc. Res. 9, 10–19.
Robinson, S.R., Dang, T.N., Dringen, R., Bishop, G.M., 2009. Hemin toxicity: a preventable source of brain damage following hemorrhagic stroke. Redox Report: Commun. Free Radical Res. 14, 228–235.
Robinson, J.L., Geser, F., Corrada, M.M., Berlau, D.J., Arnold, S.E., Lee, V.M., Kawas, C.H., Trojanowski, J.Q., 2011. Neocortical and hippocampal amyloid-beta and tau measures associate with dementia in the oldest-old. Brain: J. Neurol. 134, 3708–3715.
Sabbatini, M., Strocchi, P., Vitaioli, L., Amenta, F., 2000. The hippocampus in spontaneously hypertensive rats: a quantitative microanatomical study. Neuroscience 100, 251–258.
Sabbatini, M., Strocchi, P., Vitaioli, L., Amenta, F., 2001. Microanatomical changes of intracerebral arteries in spontaneously hypertensive rats: a model of cerebrovascular disease of the elderly. Mech. Ageing Dev. 122, 1257–1268.
Sabbatini, M., Catalani, A., Consoli, C., Marletta, N., Tomassoni, D., Avola, R., 2002. The hippocampus in spontaneously hypertensive rats: an animal model of vascular dementia? Mech. Ageing Dev. 123, 547–559.
Schreiber, S., Bueche, C.Z., Garz, C., Kropf, S., Angenstein, F., Goldschmidt, J., Neumann, J., Heinze, H.J., Goertler, M., Reymann, K.G., Braun, H., 2012. The pathologic cascade of cerebrovascular lesions in SHRSP: is erythrocyte accumulation an early phase? J. Cereb. Blood Flow Metab.: Official J. Int. Soc. Cereb. Blood Flow Metab. 32, 278–290.
Schreiber, S., Drukarch, B., Garz, C., Niklass, S., Stanaszek, L., Kropf, S., Bueche, C., Held, F., Vielhaber, S., Attems, J., et al., 2014. Interplay between age, cerebral small vessel disease, parenchymal amyloid-beta, and tau pathology: longitudinal studies in hypertensive stroke-prone rats. J. Alzheimer's Dis.: JAD 42 (Suppl 3), S205–S215.
Shen, J., Sood, R., Weaver, J., Timmins, G.S., Schnell, A., Miyake, M., Kao, J.P., Rosen, G.M., Liu, K.J., 2009. Direct visualization of mouse brain oxygen distribution by electron paramagnetic resonance imaging: application to focal cerebral ischemia. J. Cereb. Blood Flow Metab.: Official J. Int. Soc. Cereb. Blood Flow Metab. 29, 1695–1703.
Sironi, L., Tremoli, E., Miller, I., Guerrini, U., Calvio, A.M., Eberini, I., Gemeiner, M., Asdente, M., Paoletti, R., Gianazza, E., 2001. Acute-phase proteins before cerebral ischemia in stroke-prone rats: identification by proteomics. Stroke 32, 753–760.
Sironi, L., Guerrini, U., Tremoli, E., Miller, I., Gelosa, P., Lascialfari, A., Zucca, I., Eberini, I., Gemeiner, M., Paoletti, R., Gianazza, E., 2004. Analysis of pathological events at the onset of brain damage in stroke-prone rats: a proteomics and magnetic resonance imaging approach. J. Neurosci. Res. 78, 115–122.
Snyder, H.M., Corriveau, R.A., Craft, S., Faber, J.E., Greenberg, S.M., Knopman, D., Lamb, B.T., Montine, T.J., Nedergaard, M., Schaffer, C.B., et al., 2015. Vascular contributions to cognitive impairment and dementia including Alzheimer's disease. Alzheimer's Dementia: J. Alzheimer's Assoc. 11, 710–717.
Sochocka, M., Koutsouraki, E.S., Gasiorowski, K., Leszek, J., 2013. Vascular oxidative stress and mitochondrial failure in the pathobiology of Alzheimer's disease: a new approach to therapy. CNS Neurol. Disord. Drug Targets 12, 870–881.
Sood, R., Yang, Y., Taheri, S., Candelario-Jalil, E., Estrada, E.Y., Walker, E.J., Thompson, J., Rosenberg, G.A., 2009. Increased apparent diffusion coefficients on MRI linked with matrix metalloproteinases and edema in white matter after bilateral carotid artery occlusion in rats. J. Cereb. Blood Flow Metab.: Official J. Int. Soc. Cereb. Blood Flow Metab. 29, 308–316.
Stieber, A., Chen, Y., Wei, S., Mourelatos, Z., Gonatas, J., Okamoto, K., Gonatas, N.K., 1998. The fragmented neuronal Golgi apparatus in amyotrophic lateral sclerosis includes the trans-Golgi-network: functional implications. Acta Neuropathol. 95, 245–253.
Tayebati, S.K., Tomassoni, D., Amenta, F., 2016. Neuroinflammatory markers in spontaneously hypertensive rat brain: an immunohistochemical study. CNS Neurol. Disord. Drug Targets 15, 995–1000.
Ueno, M., Sakamoto, H., Tomimoto, H., Akiguchi, I., Onodera, M., Huang, C.L., Kanenishi, K., 2004. Blood-brain barrier is impaired in the hippocampus of young adult spontaneously hypertensive rats. Acta Neuropathol. 107, 532–538.
Villarreal, A.E., Barron, R., Rao, K.S., Britton, G.B., 2014. The effects of impaired cerebral circulation on Alzheimer's disease pathology: evidence from animal studies. J. Alzheimer's Dis.: JAD 42, 707–722.
Walker, E.J., Rosenberg, G.A., 2009. TIMP-3 and MMP-3 contribute to delayed inflammation and hippocampal neuronal death following global ischemia. Exp. Neurol. 216, 122–131.
Wang, W.Y., Tan, M.S., Yu, J.T., Tan, L., 2015. Role of pro-inflammatory cytokines released from microglia in Alzheimer's disease. Ann. Transl. Med. 3, 136.
Weaver, J., Jalal, F.Y., Yang, Y., Thompson, J., Rosenberg, G.A., Liu, K.J., 2014. Tissue oxygen is reduced in white matter of spontaneously hypertensive-stroke prone rats: a longitudinal study with electron paramagnetic resonance. J. Cereb. Blood Flow Metab.: Official J. Int. Soc. Cereb. Blood Flow Metab. 34, 890–896.
West, M.J., Coleman, P.D., Flood, D.G., Troncoso, J.C., 1994. Differences in the pattern of hippocampal neuronal loss in normal ageing and Alzheimer's disease. Lancet 344, 769–772.
Wong, Y.C., Krainc, D., 2017. Alpha-synuclein toxicity in neurodegeneration: mechanism and therapeutic strategies. Nat. Med. 23, 1–13.
Yamori, Y., Horie, R., Handa, H., Sato, M., Fukase, M., 1976. Pathogenetic similarity of strokes in stroke-prone spontaneously hypertensive rats and humans. Stroke 7, 46–53.
Yang, Y., Rosenberg, G.A., 2011. Blood-brain barrier breakdown in acute and chronic cerebrovascular disease. Stroke 42, 3323–3328.
Zhang, Q.G., Raz, L., Wang, R., Han, D., De Sevilla, L., Yang, F., Vadlamudi, R.K., Brann, D.W., 2009. Estrogen attenuates ischemic oxidative damage via an estrogen receptor alpha-mediated inhibition of NADPH oxidase activation. J. Neurosci. 29, 13823–13836.
Zhang, H., Shen, Y., Wang, W., Gao, H., 2015. Rat model of focal cerebral ischemia in the dominant hemisphere. Int. J. Clin. Exp. Med. 8, 504–511.
Zhao, M., Choi, Y.S., Obrietan, K., Dudek, S.M., 2007. Synaptic plasticity (and the lack thereof) in hippocampal CA2 neurons. J. Neurosci. 27, 12025–12032.